

# Identifying Three-Dimensional Radiative Patterns Associated with Early Tropical Cyclone Intensification

Frederick Iat-Hin Tam<sup>1,2</sup>, Tom Beucler<sup>1,2</sup>, James H. Ruppert Jr.<sup>3</sup>

<sup>1</sup>Faculty of Geosciences and Environment, University of Lausanne, Switzerland

<sup>2</sup>Expertise Center for Climate Extremes, University of Lausanne, Switzerland

<sup>3</sup>School of Meteorology, University of Oklahoma, Norman, OK, USA

## Key Points:

- We extract three-dimensional radiative heating patterns important to early tropical cyclone intensification from cloud-resolving simulations
- Our data-driven model pinpoints time periods where radiative heating has a dominant effect on early TC intensification
- Asymmetric anomalies in longwave radiative heating are more relevant to intensification than axisymmetric ones in our realistic case studies

## Abstract

Cloud radiative feedback impacts early tropical cyclone (TC) intensification, but limitations in existing diagnostic frameworks make them unsuitable for studying asymmetric or transient radiative heating. We propose a linear Variational Encoder-Decoder (VED) to learn the hidden relationship between radiation and the surface intensification of realistic simulated TCs. Limiting VED model inputs enables using its uncertainty to identify periods when radiation has more importance for intensification. A close examination of the extracted 3D radiative structures suggests that longwave radiative forcing from inner core deep convection and shallow clouds both contribute to intensification, with the deep convection having the most impact overall. We find that deep convection downwind of the shallow clouds is critical to the intensification of Haiyan. Our work demonstrates that machine learning can discover thermodynamic-kinematic relationships without relying on axisymmetric or deterministic assumptions, paving the way towards the objective discovery of processes leading to TC intensification in realistic conditions.

## Plain Language Summary

How clouds react to heating from the sun and Earth's surface greatly affects how quickly tropical cyclones, like hurricanes, intensify in their early stage. Traditional methods to isolate the radiative component of this effect, called Cloud Radiative Feedback (CRF), have limitations. In this manuscript, we demonstrate that machine learning can be applied to this problem and allows us to isolate, quantify, and visualize CRF with better spatial details than what is possible with traditional methods. One of the many things our machine-learning model can do is identify times when CRF is important and times when other processes are more important. Applying our model to two historical tropical cyclones shows that CRF in certain regions close to the tropical cyclones' centers are crucial for their early intensification. By using machine learning tools, we shed new light on the complex relationship between CRF and early TC intensification. This helps us understand how these storms form in real-world conditions.

## 1 Introduction

Recent advances in numerical weather prediction (NWP) models brought substantial improvements to tropical cyclone (TC) track predictions (Landsea & Cangialosi, 2018). However, predicting TC intensity (DeMaria et al., 2014; Cangialosi et al., 2020) remains challenging. One of the most elusive aspects of TC strength evolution relates to the formation ('genesis') and early intensification of TCs, which involves multiscale interaction between ambient large-scale circulation and small-scale organized convective clusters (Narenpitak et al., 2020).

Radiative feedback has been shown to be one of the leading factors in the spontaneous self-aggregation of tropical oceanic convection in non-rotating simulations of radiative-convective equilibrium (RCE; C. Muller & Bony, 2015; Wing et al., 2017; Fan et al., 2021). Including background rotation in idealized RCE experiments results in self-aggregation that forms rotating, TC-like systems (Carstens & Wing, 2020). Recent observational and modeling studies reveal four radiative feedbacks that can potentially affect TC intensity: (1) longwave environmental destabilization (Melhauser & Zhang, 2014), (2) radial gradient in radiative heating between cloudy areas and cloudless surroundings (Gray & Jacobson, 1977; Nicholls, 2015; Smith et al., 2020), (3) trapping of longwave radiation by clouds (Bu et al., 2014; Ruppert et al., 2020), and (4) diurnal radiative forcing at TC cloud anvil (Melhauser & Zhang, 2014; Ruppert & O'Neill, 2019). Processes (2) and (3) are also linked, whereby the local greenhouse trapping by clouds causes a gradient relative to cloudless surroundings. This effect is found to be particularly important in TC genesis because it creates transverse circulations that radially transport angular momentum and moisture to the inner core (Nicholls, 2015).

The effect of radiation on TC evolution is usually examined through the column Moist Static Energy (MSE) variance budget (Wing et al., 2017; Wu et al., 2021) and axisymmetric balanced dynamics (Ruppert et al., 2020; Navarro et al., 2017). Thermal forcing from diabatic processes drives the TC out of thermal wind balance; the balanced state is then restored by the secondary circulation (Willoughby, 1979). The Sawyer-Eliassen Equation (SEQ; Pendergrass & Willoughby, 2009) can diagnose such secondary circulations. However, the SEQ has limitations because it requires the TC to be in a quasi-steady state. To satisfy this condition, transient thermal forcing is smoothed out, and the SEQ solutions are only available in a two-dimensional radius-height plane. The lack of spatial (azimuthal) context makes the aforementioned frameworks suboptimal to study TC genesis pathways under shear (R. F. Rogers et al., 2020; Nam & Bell, 2021), and the role of asymmetric convection in TC intensity changes (R. Rogers et al., 2013; Zagrodnik & Jiang, 2014; Xu et al., 2017).

To address this lack of spatial context, we use machine learning (ML) models to advance our understanding of how spatial patterns affect TC intensification (McGovern et al., 2019). Specifically, we identify three-dimensional structures in radiative heating that help weak TCs intensify into stronger ones. In an ML modeling framework, these structures can be found with post-hoc attribution methods. Applying Explainable Artificial intelligence (XAI) tools to ML algorithms led to the discovery of potential vorticity patterns favoring TC rapid intensification during trough-TC interaction (Fischer et al., 2019) and outgoing longwave radiation patterns enhancing the predictability of North Atlantic extratropical circulation (Mayer & Barnes, 2021). In contrast to the post-hoc explanation method, recent studies (e.g., Barnes et al., 2022; Behrens et al., 2022) have leveraged specialized architectures akin to the Variational Encoder-Decoder architecture used in this study to find hidden structures in climate model outputs without using XAI tools, alleviating attribution uncertainty (Mamalakis et al., 2023).

Using complex ML models in scientific discovery poses notable challenges. First, these models are highly nonlinear and often not interpretable, which limits their trustworthiness. Second, complex ML models demand substantial data quantities for robust performance, which proves problematic when dealing with limited data samples. For example, we rely on limited model hindcasts in this work because finding the 3D radiative patterns relevant for genesis requires training on full 3D radiative heating structures - a variable not available in observations and reanalysis data. To address these challenges, we have developed a sparse linear model that fulfills the main traits of interpretable ML models: (i) simulability, ensuring simplicity for comprehensibility, and (ii) decomposability, meaning that the model has meaningful inputs and parameters (Lipton, 2018; Marcinkevič & Vogt, 2023).

In this research, we investigate interpretable ML models' potential to discover realistic radiative heating structures relevant to TC intensification from limited data. We offer physical insights on how these structures may contribute to early TC intensification. We will also show that uncertainties and bias in the model predictions can be used to isolate the exact period where radiative feedback is most relevant to TC intensification.

## 2 Data: Convection-permitting Hindcasts of Two Tropical Cyclones

We analyze a 20-member set of WRF (Skamarock, 2008) ensemble hindcast simulations of Typhoon Haiyan (2013) and a small set of simulations of Hurricane Maria (2017), ran at the convective-permitting resolution. The Haiyan simulations are constructed by dynamically downscaling the National Center for Environmental Prediction's Global Ensemble Forecast System (GEFS) ensemble member outputs. The main source of variability in the Haiyan ensemble involves the multiscale interaction between convection and the slight variability in the GEFS outputs' synoptic conditions. The Haiyan WRF sim-

ulations are integrated from November 1, 2013, 00 UTC to November 8, 2013, 00 UTC, with a triple-nested, 27km-9km-3km horizontal grid spacing model domain. Radiation is treated with the Rapid Radiative Transfer Model for GCMs (RRTMG; Iacono et al., 2008) and microphysics is treated using the Thompson and Eidhammer scheme (Thompson & Eidhammer, 2014). The model contains 55 stretched vertical levels and is topped at 10 hPa. These simulations are assigned integer labels from 0 to 19. The simulations for Maria are identical to those introduced in Ruppert et al. (2020), and test the effect of cloud radiation on TC intensification. This set of simulations includes one Control (CTRL) experiment and 4 “no Cloud Radiative Feedback” (“no-CRF” for short) sensitivity simulations. “No-CRF” simulations are produced by running the CTRL restart files at different times, albeit disregarding all hydrometeor when calculating infrared and solar radiation. These simulations are initialized from GEFS analysis and integrated from September 14, 2017, 1200 UTC to September 20, 2017, 1200 UTC.

All simulations produce outputs at an hourly interval; these outputs are post-processed into a TC-relative framework by tracking the local maxima in 700-hPa absolute vertical vorticity, spatially smoothed with a 1.5-degree boxcar filter, and temporally filtered with a 3-point Gaussian filter to remove noise.

Following best machine learning practices, we split the data into training, validation, and test sets. The splitting strategy for both TCs is experiment-based. Two members not strongly correlated to the others are first left out for testing. We then perform a randomized removal of 2 members to create the validation set, with the remaining 16 members used for training. We repeat the cross-validation procedure multiple times to fully sample the sensitivity of model skill to validation folds. Two CRF sensitivity experiments are left out for Maria as validation and test sets. The remaining three simulations constitute our training set. All Maria models reported here are tested on the “NCRF-36h” sensitivity simulation.

For conciseness, the analysis for Haiyan focuses on two ensemble members: Member 2, which intensifies at a quicker rate, and Member 11, which intensifies at a slower rate.

### 3 Methodology

Our analysis leverages machine learning to identify spatial features in the WRF outputs relevant to TC intensification. We adopt an interpretable, stochastic linear variational encoder-decoder (VED) to discover such features. A schematic diagram of our framework is provided in Fig 1. The learned encoder incorporates Principal Component Analysis (PCA) to compress three-dimensional WRF longwave radiation and shortwave radiation outputs into multiple low-dimensional PCs suitable for shallow ML models. A linear regression layer in the encoder combines the PCs into traceable compressed representations that result in skillful TC intensity forecasts. The purpose of the linear encoder is to distill all physical information relevant to TC predictability in different PCs into a single structure, which makes the model more interpretable and avoids overfitting. The temporal evolution of the compressed structures is used to predict the 24-hour intensification of TC surface intensity with a linear decoder.

There are two critical assumptions in the model architecture. First, we predict intensification with only the longwave and shortwave radiation information. It is unlikely that all pathways to tropical cyclone genesis and intensification are included in this simplified, underdetermined system. We adopted this strategy because we are in a low sample regime, which means restricting and simplifying the input helps avoid model overfitting. However, we believe the highly restricted nature of the model creatively yields physical understanding. Specifically, we argue that the temporal evolutions of model spread and error reveal the changes in the relevance of radiation with time. Large spread and

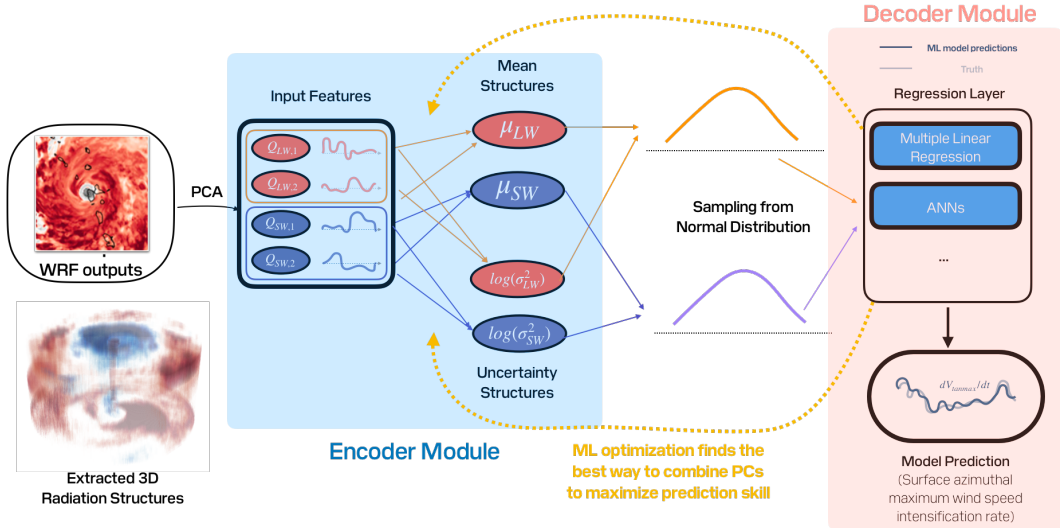


**Figure 1.** The interpretable linear VED framework proposed in this study combines a pattern-finding encoder and a decoder for TC intensification rate prediction. The first linear layer in the encoder modules combines different radiation structural information in the PCs into the time evolutions of the mean structures and uncertainty structures. A random sampling of the normal distributions with mean and log variances conditioned on the inputs introduces uncertainty to the linear decoder 24-hour surface wind intensification prediction module. Optimization of model weights with loss functions tries to minimize the absolute error between the truth and the predictions from the decoder based on the learned patterns.

errors should arise when the system is undetermined and requires information from non-radiative variables for reliable intensification predictions. These are periods where non-radiative processes are strong predictors of TC intensification. In contrast, we expect smaller model errors and spread when TC intensification is more strongly coupled to radiative heating. Second, we assume that the TC intensification rate is linearly related to the learned radiative heating structures. This decision is justified in our problem because sensitivity tests with nonlinear layers added to the decoder did not improve model skills. However, introducing nonlinearity to the regression layer may be beneficial when applying this framework to other problems. These assumptions are also supported by prior studies that show strong, first-order sensitivity of TC intensification to the removal of radiative feedback (e.g., Ruppert et al., 2020; Smith et al., 2020).

The proposed VED structure enables uncertainty quantification for both the latent representations and the final prediction. The VED architecture introduces uncertainties into the model to predict the full distribution of compressed radiative structures and their corresponding intensification rates. The linear encoder computes and stores the mean ( $\mu$ ) and logarithmic variances ( $\log \sigma^2$ ) of the longwave and shortwave latent structure distributions in four nodes. A “reparameterization trick” is used to create normal distributions based on the  $\mu$  and  $\log \sigma^2$  (Kingma & Welling, 2022). Here, we use  $\log \sigma^2$  rather than  $\sigma^2$  for training stability. The two radiative latent features ( $Z$ ), obtained by randomly sampling the normal distributions, are used as inputs to the linear decoder for intensification rate predictions, which introduces uncertainties to the model prediction. By providing the full distribution of possible latent structures and likely prediction outcomes, the models are more trustworthy and can be reliably interpreted, which is crucial when we use data-driven techniques to discover new physical processes. For exam-

ple, uncertainties in the predictions can be used to assess the relevance of radiation with time, whereas uncertainties in the latent structures highlight specific areas in the structure to focus on for scientific discovery. In the subsequent sections, we provide examples of adopting the above strategy to identify when radiation matters to the two simulated TCs and where the radiative anomalies matter the most to their intensification.

We show in SI1.1 that our VED probabilistically predicts surface wind intensification through the following equation:

$$\underbrace{\frac{dV_{\text{surf}}}{dt}}_{\text{Intensification}} = b + \underbrace{a_{\text{LW}} \cdot \mathcal{N}(\mu_{\text{LW}}, \log \sigma_{\text{LW}}^2)}_{\text{Longwave contribution}} + \underbrace{a_{\text{SW}} \cdot \mathcal{N}(\mu_{\text{SW}}, \log \sigma_{\text{SW}}^2)}_{\text{Shortwave contribution}}, \quad (1)$$

where  $V_{\text{surf}}$  is the maximum tangential mean surface winds in units of m/s,  $dV_{\text{surf}}/dt$  its time-tendency in m/s<sup>2</sup>, here approximated by the 24 hr-change in  $V_{\text{surf}}$ ,  $(a_{\text{LW}}, a_{\text{SW}})$  linear regression coefficients in m.s<sup>-1</sup>.K<sup>-1</sup>, and  $b$  the intercept in m/s<sup>2</sup>, which can be thought of as the intensification's expected value over the training set (positive in our case). By construction, the moments of the normal distributions are related to linear projections of the radiative heating field anomaly  $\text{LW}'$  on data-driven, stationary patterns whose spatial structure can be used to interpret our model. For example, the conditional mean of the normal distribution used to estimate the longwave contribution,  $\mu_{\text{LW}}$ , can be expressed as the projection of the spatiotemporal longwave heating field onto a stationary, unitless, and normalized pattern  $\Pi_{\mu_{\text{LW}}}$ :

$$\underbrace{\mu_{\text{LW}}(t)}_{\text{Conditional Mean}} = \left\langle \underbrace{\text{LW}'(x, y, z, t)}_{\text{Longwave Heating Anomaly}} \mid \underbrace{\Pi_{\mu_{\text{LW}}}(x, y, z)}_{\text{Data-Driven Pattern}} \right\rangle. \quad (2)$$

We use the same technique and consistent notation for the shortwave contribution. In the prediction equation, positive longwave contributions to surface wind intensification arise when the values sampled from  $\mathcal{N}(\mu_{\text{LW}}, \sigma_{\text{LW}})$  are greater than zero. Positive longwave or shortwave contributions will lead to intensification quicker than the training set reference ( $b$ ), and vice versa. A quicker intensification occurs when the spatial distribution of longwave anomaly relative to the training average projects strongly onto  $\Pi_{\mu_{\text{LW}}}$ . In contrast, smaller intensification rates correspond to cases in which longwave anomalies and  $\Pi_{\mu_{\text{LW}}}$  are orthogonal with respect to the scalar product (see SI1.1 for details). Other details of the model training processes are discussed in SI1.2-1.4.

To understand how the VED performs compared to traditional baselines, we designed a two-branch principal component regression model with Monte-Carlo Dropout that also gave learned structures uncertainties. The best VED model captures the TC intensification rates better than the best PC regression model, with a better-calibrated uncertainty in the final predictions (see SI1.5-1.6 for details).

## 4 Results

An advantage of our proposed model architecture is that it simultaneously extracts structures relevant to 24-hour intensification rates and the uncertainties in the predictions. Here, we explore using this information to understand (i) how we can use ML to identify temporal periods where radiation is an important driver of intensification, (ii) the relevance of axisymmetric radiation to intensification, (iii) whether asymmetric radiation exerts influence on intensification, and (iv) whether we can show this influence with simple perturbation experiments.

## 4.1 Prominence of Radiative Feedbacks in the Early Intensification Phase

### 4.1.1 Identifying Periods of Radiatively-Driven Intensification

By construction, our simple VED model predicts TC intensification exclusively from radiative heating, overlooking significant contributions from surface fluxes and wind-induced surface heat exchange (Zhang & Emanuel, 2016; Murthy & Boos, 2018). Recent modeling studies (e.g., Smith et al., 2020; Yang & Tan, 2018) suggest that radiative heating could be less critical to TC intensification beyond the initial genesis or spin-up stage.

To investigate whether this holds in our case studies, we use the VED model to *identify periods when TC intensification is dominated by radiative feedback*. Instances with large model errors or uncertainties are times when radiative heating alone cannot predict TC intensification, whereas instances with accurate predictions and minimal uncertainty are likely times when radiative heating is dominant.

This capability of our VED to distinguish radiative heating-dominated stages is crucial for reliability assessment and scientific discovery. Figure 2 presents the mean prediction and prediction spread of the best-calibrated VED models for Haiyan and Maria. For Maria, the probabilistic ML models replicate the intensification rate reduction in CRF mechanism-denial experiments (Fig. 2a). Decomposing predicted intensification into longwave and shortwave contributions (Fig. 2b) shows that the slower intensification in the mechanism-denial experiments is primarily attributable to the longwave component. This result is reassuring as it identifies the longwave component of CRF as the main contributor to the early intensification of TCs, consistent with the “cloud greenhouse effect” framework in Ruppert et al. (2020). However, the model underestimated the intensification rate at the latter stage of the NCDF60 TC’s life cycle, possibly due to unaccounted non-radiative processes like the surface fluxes feedback (e.g., Zhang & Emanuel, 2016). Furthermore, the model assigned a smaller weight to the shortwave channel in the linear prediction equation for Maria (Fig. 2b). We believe the model has learned the strong effect of disabling CRF in the sensitivity experiments and its effect on intensification, which manifests mostly in the longwave channel. The shortwave contribution is larger in the realistic Haiyan ensemble simulations (Fig. 2d).

For Haiyan, where CRF always exists, we compare the VED predictions for a high intensification rate Haiyan ensemble member (Member 2) to those for a slow intensification member (Member 11) to assess the role of radiation in realistic conditions (Fig. 2c). Increased bias (Fig. 2c) and wider uncertainty range (Fig. 2e) for Member 2 predictions in the latter part of the TC’s life cycle shows the limitation of the VED model to understand the mature phase of TC intensification. The prediction distribution for samples taken during the high uncertainty phase is close to the training data distribution (the prior), implying the need for non-radiative inputs to adequately constrain the probabilistic predictions and reduce overall model bias. In contrast, the model predictions for samples taken from the early intensification phase of Member 2 are accurate, indicating predictability from the radiative heating fields.

Comparing linear decompositions of VED predictions (Fig. 2d) reveals that lower intensification rates for Member 11 (Hours 10-20) are due to reduced longwave contribution. Positive longwave contribution in Member 2 leads to a faster intensification rate beyond the persistence baseline. In the next section, we analyze the radiation structures in the two ensemble members to illustrate how differences in radiative heating structures can explain their differing intensification rates.

### 4.1.2 Qualitative Agreement with Existing Diagnostic Tools

In the previous section, we claimed that the transition from an accurate, low-uncertainty regime to an inaccurate, high-uncertainty regime in the VED predictions can be under-

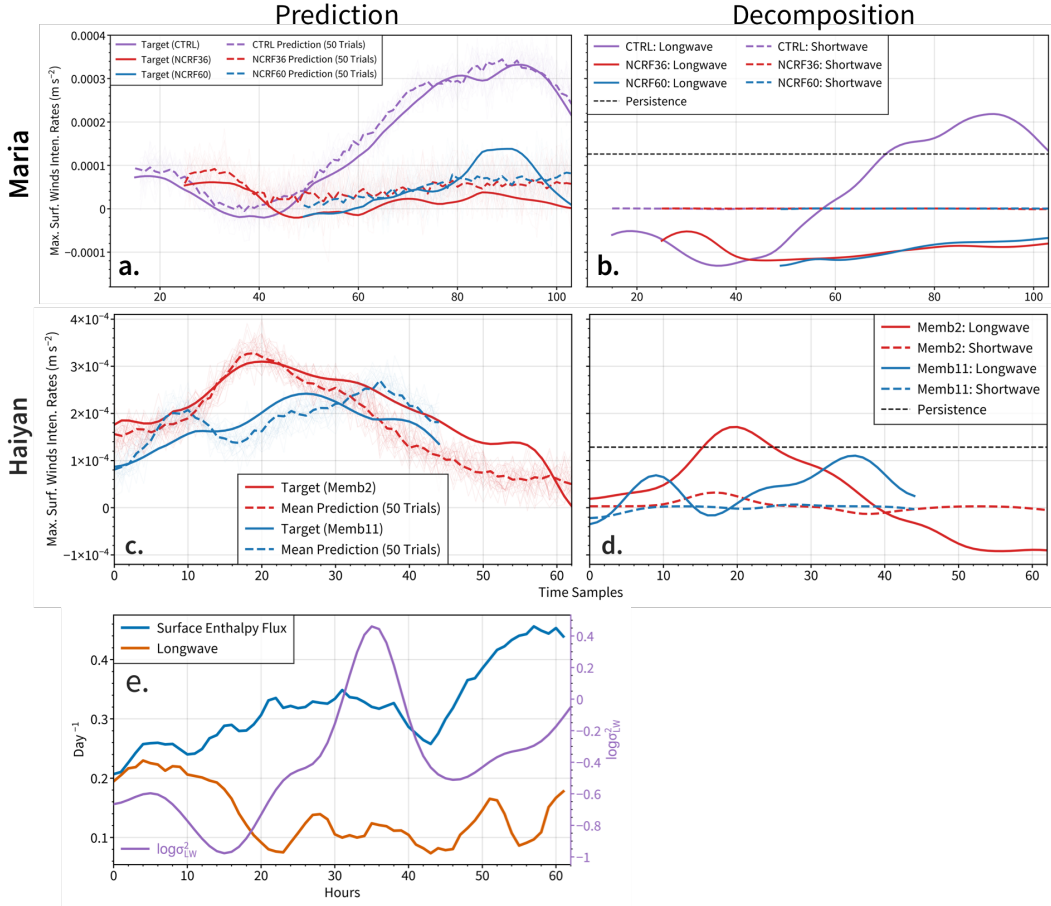


**Figure 2.** Decomposing tropical cyclone intensification predictions for Maria and Haiyan shows longwave radiative heating's link to early intensity differences. We present mean VED surface intensification predictions (dashed) for Maria (a) from three WRF simulations and for Haiyan (c) from two ensemble members, with actual intensities (thick). Panels (b) and (d) show longwave and shortwave radiation contributions. Panel (e) explores the evolution of longwave-related uncertainty (purple) against two MSE variance sources (blue and brown). In Maria's mechanism-denial experiment and the early phase of Haiyan, the model associates the difference between a quickly intensifying TC and a slowly intensifying one with longwave radiation.

stood as separating periods where radiation is more important from ones where non-radiative processes are more important. Here we use well-established diagnostic tools to evaluate to what extent the claim is true.

The cyclogenesis process can be thermodynamically tracked using the Frozen Moist Static Energy Spatial Variance Budget (Wing & Emanuel, 2014; C. J. Muller & Romps, 2018; Carstens & Wing, 2020):

$$\frac{1}{2} \frac{\partial \text{var} \hat{h}}{\partial t} = \underbrace{\overline{\hat{h}' \text{LHF}'} + \overline{\hat{h}' \text{SHF}'}}_{\text{SEF Contribution}} + \underbrace{\overline{\hat{h}' \text{NetLW}'} + \overline{\hat{h}' \text{NetSW}'}}_{\text{Radiative Contribution}} - \overline{\nabla_h \cdot \vec{u} \hat{h}}, \quad (3)$$

where  $\text{var} \hat{h}$  is the spatial variance of vertically integrated moist static energy, and SEF (the Surface Enthalpy Flux) is the sum of LHF (the Latent Heat Flux) and SHF (the Sensible Heat Flux). The radiative contribution consists of net column longwave radiative flux convergence (NetLW) and net column shortwave radiative flux convergence (NetSW). Primes are used to indicate anomalies relative to the mean of the spatial domain, which is represented by overlines. MSE spatial variance source terms are obtained by spatially averaging all terms on the right hand side of Equation 3. We perform the spatial averaging from 0 to 600 km from the TC center. A detailed description of the MSE variance budget is provided in SI Section 3. The MSE variance summarizes the spatial distribution of frozen MSE surrounding a developing tropical cyclone, with the biggest contribution coming from moisture. Since tropical cyclogenesis shares similarities with rotating convective self-aggregation, TCs form as the TC thermodynamics transition to an aggregated state, characterized by a compact moisture blob surrounded by drier air (positive  $\partial_t \text{var} \hat{h}$ , e.g., C. J. Muller & Romps, 2018; Carstens & Wing, 2020). From Equation 3, the source terms for the MSE variance are the covariance between the existing MSE anomalies and different flux anomalies. Creating positive MSE variance anomalies necessitates spatially-aligned anomalies. For example, positive radiative contribution to MSE variance may arise from warm longwave heating anomaly in the high energy TC inner core or cool radiative anomalies in the drier TC surroundings (Nicholls, 2015). Inward moisture transport from radiatively-driven secondary circulations (e.g., Nicholls, 2015; Ruppert et al., 2020; Smith et al., 2020) can enhance MSE variance by redistributing moisture towards the TC center.

Here we use the MSE variance budget to validate the claim, based on ML prediction uncertainties, that the realistic Haiyan simulations shift from a radiatively-dominated early intensification phase to a non-radiative-dominated one. Fig 2e compares the time evolution of the MSE variance source terms and the time evolution of the learned logarithmic variance structure for the longwave channel ( $\log \sigma_{LW}^2$ ). Focusing on Haiyan member 2, the contribution from NetLW to the overall MSE variance budget is initially comparable to the contribution from SEF. However, longwave radiation steadily becomes less important towards the end of the time series, consistent with the expected behavior of intensifying TCs, with an increase in prominence of non-radiative feedback after the initial genesis stage. Two distinct phases emerge in the  $\log \sigma_{LW}^2$  time series, one with smaller values initially and one with larger values shortly after. The comparison shows that we can use the interpretable ML framework to draw physical insights akin to existing diagnostic frameworks. A notable caveat to the above discussion is that our ML framework predicts TC kinematic changes, whereas the MSE variance budget measures thermodynamical changes. This distinction potentially explains the time lag between the decrease in longwave contribution to MSE variance and the increase in ML prediction uncertainties. The idea that thermodynamic forcing precedes kinematic changes can be supported by Figure 2 in Ruppert et al. (2020), where TC surface intensification occurs 12-24 hours after the drop in SEF contributions. The analysis in Tang (2017) also shows that strong moist entropy forcing precedes the genesis time of idealized axisymmetric TCs. Finally, airborne observations suggest that the TC core becomes and remains close to saturation for some time before the build-up of storm circulations (Bell & Montgomery,

2019). In summary, the available evidence suggests that TC thermodynamic change is a precursor to TC circulation change, partially supporting our interpretation of the time lag seen in Fig.2e.

## 4.2 Axisymmetric results: The dominance of upper-level longwave radiation

The proposed framework's physical interpretability relies on the model predictions, extracted mean structures, and extracted uncertainty structures. In the following sections, we progressively highlight different aspects of the extracted structures to show how they can clarify the role of radiation in TC intensification. We start by analyzing the azimuthal mean of VED-extracted structures to illustrate how spatial gradients in radiative anomalies affect TCs.

### 4.2.1 *Maria*

In the case of the *Maria* simulations (Figure 3), the VED model extracts a  $\mu_{LW}$  pattern with an upper-level longwave anomaly dipole and a shallow cloud radiative signal near the surface (Figure 3c). The anomaly fields are defined with respect to the training mean. In other words, it shows how the radiative heating structure of a sample deviates from the mean of all training samples. This way of defining the anomaly also eliminates the need to recalculate the PCs for individual experiments. To demonstrate how the learned  $\Pi_{\mu_{LW}}$  (Fig. 3c) encodes physical knowledge, we compare Hour 50 from the *Haiyan* CTRL simulation (Fig. 3a, b) to a sample taken from the same time in the NCRF-36h experiment (Fig. 3d, e). The VED framework predicts a higher surface intensification rates for the CTRL sample due to positive  $\mu_{LW}$ , whereas the NCRF-36h sample has a smaller predicted intensification rate due to negative  $\mu_{LW}$ . Comparing Figure 3b and c, we see that a positive  $\mu_{LW}$  arises when the anomaly field is spatially distributed in the same way as  $\Pi_{\mu_{LW}}$ . In the raw longwave radiation field (Fig. 3a), the  $LW'$  of the CTRL sample corresponds to the concentration of strong longwave cooling near the cloud top and heating near the TC center. In contrast, the negative  $\mu_{LW}$  in the mechanism denial example features a lowered and weakened longwave cooling and a completely absence of heating near TC center, both contributes to a weaker simulated TC. From the *Maria* example, we demonstrate that combining the sign of the projection ( $\mu_{LW}$ ) and the raw fields provide useful information on why NCRF-36h TC fails to intensify. In the next section, we use  $\mu_{LW}$  to understand why two *Haiyan* ensemble members have different intensification rates during their organization phases.

### 4.2.2 *Haiyan*

The azimuthal mean of  $\mu_{LW}$  for *Haiyan* (Figure 4c) exhibits a vertical dipole pattern around 200 hPa and a shallow vertical dipole at 900 hPa, reflecting broad anvil clouds in the outer core and shallow clouds in the inner core. We compare samples from two members: Member 2, with a significant positive  $\mu_{LW}$  (larger predicted intensification rate), and Member 11, with a small  $\mu_{LW}$  (smaller predicted intensification rate). In the Member 2 sample, positive  $\mu_{LW}$  indicates weakening of the upper-level longwave dipole between 50 km to 300 km from the TC center and a vertically expanded upper-level longwave heating near the TC center, along with a more prominent 900 hPa shallow cloud radiative dipole. These longwave patterns may indicate deep convective development, rising outflow height near the TC center, destabilized inner core upper-level thermal stratification, and enhanced shallow cloud frequency. Colder upper tropospheric temperatures and higher outflow layers have been shown to boost TC intensity. Following balanced dynamics (Eliassen, 1952; Pendergrass & Willoughby, 2009), upper-level radiative cooling triggers secondary circulations that accelerate surface tangential winds in idealized TCs (Trabing et al., 2019). From an energetic perspective, rising outflow layers enhance

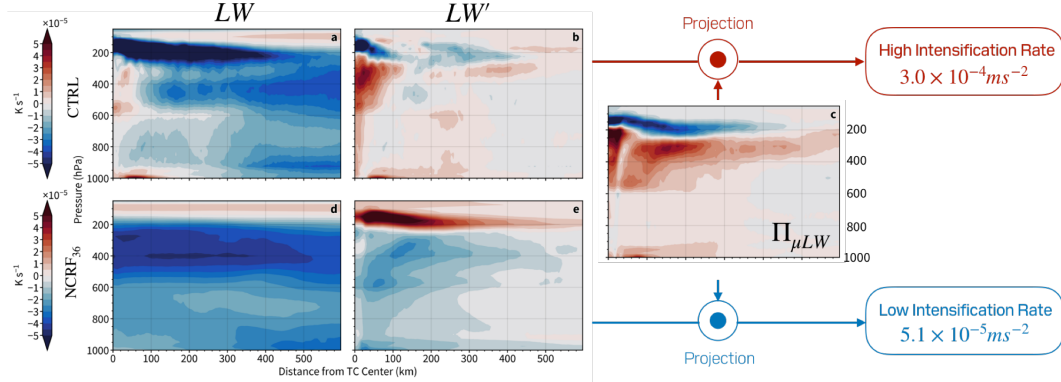


**Figure 3.** The learned data-driven structure for the mean longwave prediction ( $\Pi_{\mu LW}$  from Maria c) shows that CRF creates a prominent upper-level longwave anomaly dipole *compared to the training mean* in a sample taken from the CTRL simulation ( $LW'$ ; a,b) and increases the predicted TC intensification rates. The example in the upper row is taken from Hour 80 of the CTRL simulation, which has a higher predicted surface intensification due to a positive projection of  $LW'$  onto  $\Pi_{\mu LW}$ . The lower row shows at the same hour from the NCRF-36h simulation, which has a negative projection onto  $\Pi_{\mu LW}$ .

the thermal efficiency of a TC heat engine, resulting in a stronger TC (Ramsay, 2013; S. Wang et al., 2014). While shallow clouds are suggested to assist cyclogenesis by moistening the lower troposphere and spinning up the near-surface circulation (Z. Wang, 2014), our VED model analysis implies their effect on the overall TC intensification is relatively minor. Decomposing the model prediction by vertical level suggests that the shallow cloud contribution to intensification is between two and one order of magnitude smaller than the upper-level radiative contribution (see SI Section 2 for details). These findings corroborate those from idealized simulations (e.g., Kilroy, 2021).

#### 4.3 Asymmetric Radiative Heating favors Tropical Cyclone Intensification

Here, we show that asymmetric longwave radiative anomaly structures are potential predictors for intensification and that we can identify regions within these structures most associated with intensification using the uncertainties in the learned mean structures. The linear combinations of PC longwave eigenvectors yield a complex, spatially asymmetric, three-dimensional radiative heating pattern (Fig. 5a,b). The  $\Pi_{\mu LW}$  cross sections at 1000 hPa (Fig. 5a) and 100 hPa (Fig. 5b) both exhibit distinct wavenumber-1 asymmetry, with the shallow cloud radiative signature at 1000 hPa (i. in Fig. 5a) distributed upwind of the deep convective signature at 100 hPa (ii. in Fig. 5b). These results suggest that the shallow clouds likely still play a role in intensifying *local* winds, despite a minor contribution to the overall TC intensification (Section 4.2).

To identify inner-core radiative anomalies that are unambiguously correlated to surface intensification, we create standard deviation maps from the 10 best-performing models'  $\Pi_{\mu LW}$  structures (Fig. 5d,e). At 1000 hPa, the models are in broad agreement with a cold LW anomaly at the TC center and a shallow cloud signature to the southeast of the TC center (Fig. 5c). However, a high standard deviation in the transition zone between the two areas indicates uncertainty in the spatial extent of these signatures across models. At 100 hPa, the smallest standard deviation in the inner core coincides with the deep convective warm LW anomaly immediately downwind of the shallow cloud signature and south of the TC center (Fig. 5d). Taking these results into account, we sum-

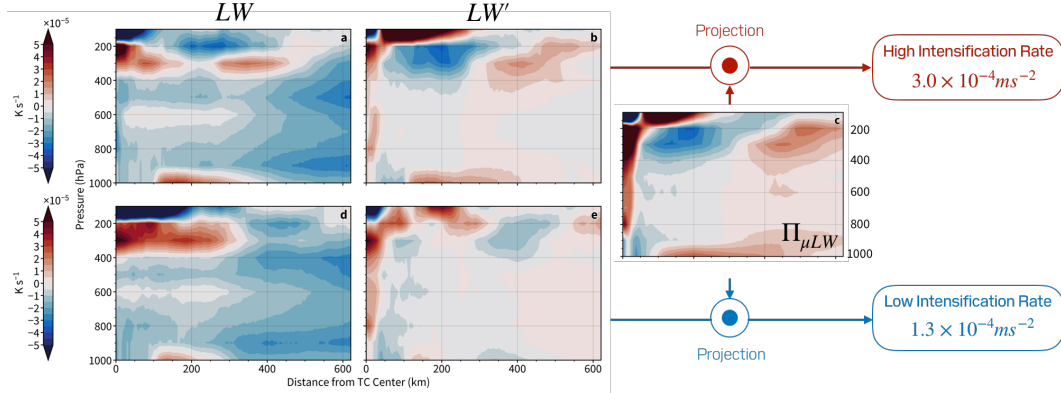


**Figure 4.** The learned data-driven structure for the mean longwave prediction ( $\Pi_{\mu LW}$  in panel c) shows that radially-extended axisymmetric longwave anomalies ( $LW'$ ; b,d) are associated with larger TC intensification rates. The example in the upper row is taken from Hour 15 of Member 2, which has a higher predicted surface intensification due to a positive projection of  $LW'$  onto  $\Pi_{\mu LW}$ . We contrast the Member 2 example with the Hour 17 of Member 11 (d, e), which is predicted to intensify more slowly due to a close to zero projection onto  $\Pi_{\mu LW}$ .

marize that the deep convection downwind of the low-troposphere shallow cloud signature likely has the strongest link to surface intensification.

Considering how upper-level longwave cooling anomalies may be associated with intensifying tangential winds through secondary transverse circulations, we postulate that any positive longwave contribution to Member 2 surface winds should be distributed mostly in the TC's northern half. We validate this by the spatial distribution of the surface wind intensification from Hour 16 to 40 (Fig. 5c), which shows the effect of a positive  $\mu_{LW}$ . The surface wind acceleration is indeed broader over the TC's northern half, with the strongest acceleration located downwind of the positive upper-level  $\Pi_{\mu LW}$  with minimal uncertainty. The spatial correlation between surface wind acceleration and  $\Pi_{\mu LW}$  supports the hypothesis that upper-level wavenumber-1 longwave heating anomaly contributes positively to surface intensification. We also observe a strong spatial correspondence between the shallow cloud signature and upper-level convective signature, which hints at a possible link between the two features. Finally, widespread inner core convective development near and slightly downwind of the upper-level longwave anomalies points to a link between longwave anomalies, secondary circulations, and deep convective development, which also facilitate the axisymmetrization of TC structures - an indicator of TC genesis (Hendricks et al., 2004) and intensification (Shimada et al., 2017).

#### 4.4 Outlook: Anticipating the response of tropical cyclones to radiative perturbations

One of the main advantages of ML models compared to traditional physics-based models is that ML models are inexpensive to run once they are trained. This characteristic of ML models may be leveraged for scientific discovery. Specifically, we believe that ML models can be treated as an efficient hypothesis generator and a framework in which simple hypothesis testing can be made.

We design a sensitivity experiment to use the trained Haiyan models to understand whether the prominent wavenumber-1 structure in  $\mu_{LW}$  means that asymmetric longwave anomaly is truly more important to intensification than axisymmetric ones. These questions are easily answerable by feeding the ML models with perturbed input, i.e., syn-

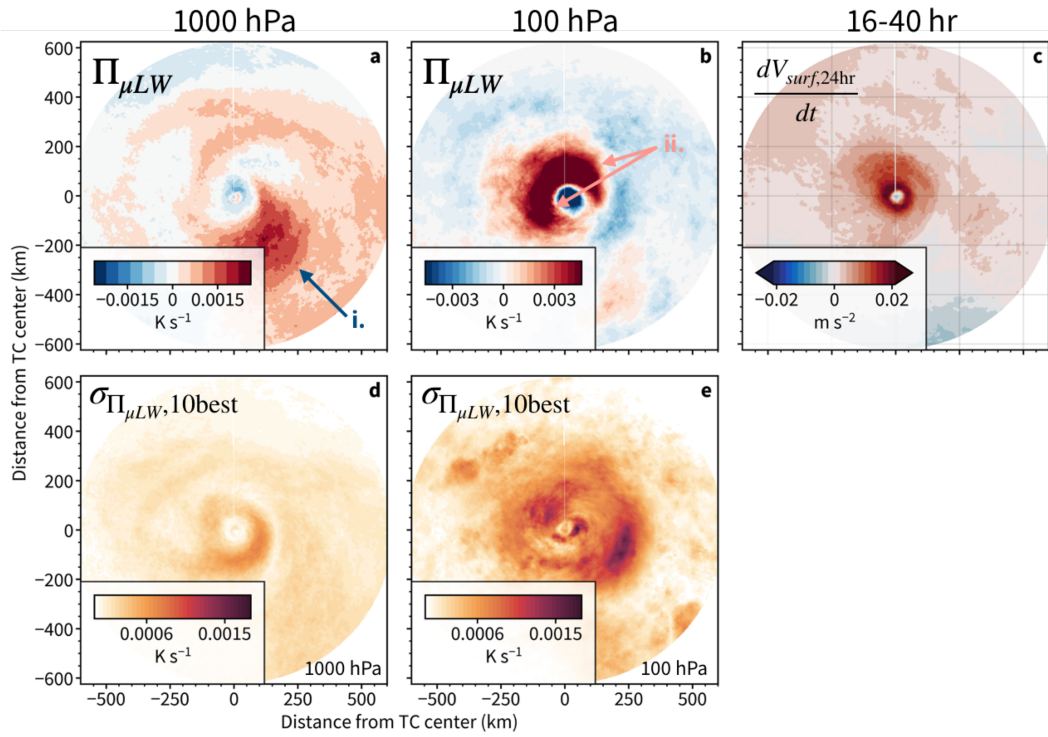


**Figure 5.** The spatial cross-sections of the best-performing model's mean longwave pattern  $\Pi_{\mu LW}$  at (a) 1000 hPa, and (b) 100 hPa show high degree of spatial asymmetry in the inner core. The trustworthiness of different anomaly areas in  $\Pi_{\mu LW}$  is assessed by the standard deviation of the 10 best models'  $\Pi_{\mu LW}$  (1000 hPa, c; 100 hPa, d). The strongest (e) 24-hr surface intensification is located downwind of the upper-level longwave heating anomaly with low structural uncertainty (ii in panel b).

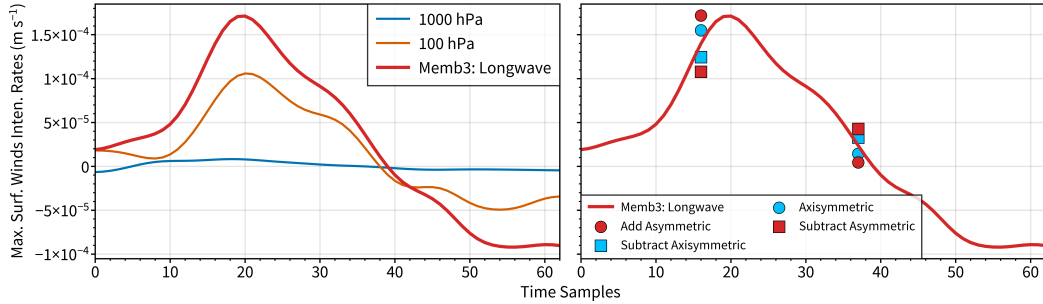


**Figure 6.** Providing the trained ML models with perturbed inputs gives us the first hints as to how the tropical cyclones might behave in a true intervention setting. Perturbed input experiments show that adding and subtracting the asymmetric  $\Pi_{\mu LW}$  from inputs (red dots and squares) to the inputs change the ML prediction for a given sample more than when an axisymmetric version of  $\Pi_{\mu LW}$  is added to or removed from the inputs (blue dots and squares).

thetic structures. Here, we present the full definition of axisymmetric and asymmetric anomalies used in the intervention experiments.

Taking longwave radiation as an example, its mean contribution to the ML intensification forecast is proportional to:

$$\langle LW' | \Pi_{\mu LW} \rangle_{LW} \quad (4)$$

We would like to show that adding an asymmetric pattern like  $\Pi_{\mu LW}$  causes the ML model to predict higher intensification rates than adding an axisymmetric pattern. In the asymmetric pattern experiment, we perturb the raw data in cartesian coordinates by adding the learned pattern to the training-mean longwave cooling field:

$$\overline{LW_{\text{training}}} \pm \Pi_{\mu LW}, \quad (5)$$

which tests the effect of adding or removing extra radiation to specific areas in the developing TC. For the case of the axisymmetric pattern experiment, we perturb the raw data with the azimuthal mean of the extracted  $\mu_{LW}$  pattern:

$$\overline{LW_{\text{training}}} \pm \gamma \overline{\Pi_{\mu LW}}^{\theta}, \quad (6)$$

where  $\gamma$  is a multiplication factor that ensures that both synthetic structures have the same spatial variance and  $(\cdot)^{\theta}$  is the azimuthal mean operator. In practical terms, every grid point in the axisymmetric synthetic structure is multiplied by the ratio between the standard deviation of the asymmetric and axisymmetric synthetic structure.

When the VED is fed the new inputs perturbed by synthetic asymmetric structure, it predicts higher longwave contributions to intensification during the early intensification stage. Conversely, the axisymmetric synthetic structure leads to a smaller response in the VED prediction (Fig. 6). VED predictions are only weakly sensitive to the synthetic perturbations later in the TC's life cycle. These results broadly agree with our conjecture that asymmetric longwave forcing leads to faster early TC intensification in the data-driven models.

## 5 Conclusion

Recent evidence (e.g., Ruppert et al., 2020) highlights the significance of radiation in early TC development. However, the precise role of radiation in realistic TCs and

whether asymmetric structures in radiation impact TCs differently from axisymmetric ones has remained underexplored. We fill this knowledge gap by employing a data-driven, interpretable, stochastic, machine learning model (VED) on convective-permitting simulations of two TCs to estimate the transfer function between 3D radiative patterns and surface wind intensification. We optimize the model architecture to enhance the likelihood of extracting physically meaningful patterns. This optimization involves (i) maximizing surface intensification prediction skills by optimally combining different asymmetric radiative patterns, and (ii) regressing to the unconditional distribution of intensification rates when radiation is uninformative. In both case studies, our model finds spatially coherent, physically meaningful radiation patterns from complex, high-dimensional simulation output data.

The VED architecture allows the quantification of uncertainties in both the model predictions and the extracted radiation patterns. We provide several examples where this information can be leveraged for scientific discovery. By intentionally making the model learn exclusively from radiation, the errors and uncertainties in ML predictions are quantifiable indicators of how relevant radiation is to TC intensification. Our findings reveal that longwave radiation exerts a larger influence on intensification than shortwave. The radiation is mostly only relevant in the early genesis phase, consistent with the results from prior physical modeling experiments.

The ML model extracts three-dimensional structures in radiation and quantifies the effect of different radiative anomalies on intensification. Our results suggest that the combination of inner-core deep convective development and near-surface shallow clouds may be used as useful predictors for the rate of intensification during the TC genesis phase. We further show that both the upper-level deep convective signal and the near-surface shallow cloud signal have a wavenumber-1 spatial asymmetry. Our VED model's linearity is useful here because we can e.g., decompose by vertical level to conclude that the upper-level radiative signal likely impacts the surface intensification the most. The VED-extracted three-dimensional longwave anomaly structure for Haiyan has a strong spatial correlation with the broader surface wind intensification in the northern quadrants, which is potentially useful to highlight where longwave radiative anomalies should be distributed that can potentially yield the most impact on TC intensification.

We believe that the strength of the ML framework here lies in its simplicity. The fully linear nature of the model ensures full interpretability and decomposability, providing clarity on how the model extracts structures from WRF outputs. Our case studies demonstrate the value of sacrificing some model performance for interpretability and how interpretability leads to scientific discovery. Our approach is a useful addition to existing data-driven approaches for scientific exploration and is particularly useful in situations with limited training data. The architecture is flexible, allowing for an easy introduction of nonlinearity and making it adaptable to other prediction problems in more complex systems.

Looking ahead, interpretable ML architectures can potentially be used to (i) reveal the source of forecast spreads in ensemble model predictions for extreme winds, e.g., by identifying the dominant uncertainty-adding circulation patterns, and (ii) quantifying the impact of different physical variables on uncertainties in climate models. Finally, a logical next step to build trust in the ML model explanations is to use the learned structures for targeted sensitivity experiments with physics-based numerical models, which should clarify the causal relationship between these structures and TC intensification.

## 6 Open Research

The code used to train the neural networks and to produce all figures of this manuscript is hosted on Github ([https://github.com/freddy0218/2024\\_TCG\\_VED](https://github.com/freddy0218/2024_TCG_VED)). The processed

PC time series data, trained models are archived on a Zenodo public repository (Tam, 2024). The post-processed longwave and shortwave WRF radiation fields for the two Haiyan ensemble members are also included in the archive for recreating the results shown in Figure 2 and 4. The WRF model simulations used in this work are available upon request. The PyTorch (Paszke et al., 2019) framework is used to train all the machine learning models in this manuscript. The binary files of PyTorch are available for installation via the Anaconda platform. The Optuna optimization tool can be accessed on <https://github.com/optuna/optuna>. We provide a short Jupyter tutorial with the minimal steps required to use the trained models to get the intensification rate predictions and the extracted mean longwave structure.

### Acknowledgments

This research was supported by the canton of Vaud in Switzerland. J.H.R. acknowledges funding support from the National Science Foundation under grants AGS 1712290 and 2331120. The authors acknowledge the Scientific Computing and Research Support Unit (DCSR) and Dr. Margot Sirdey at the University of Lausanne for providing the necessary computational resources and technical support. The authors also acknowledge Dr. Saranya Ganesh S., Mr. Milton Gomez, and Mr. Louis Poulain-Auzéau for fruitful discussions.

### References

Barnes, E. A., Barnes, R. J., Martin, Z. K., & Rader, J. K. (2022). This looks like that there: Interpretable neural networks for image tasks when location matters. *Artificial Intelligence for the Earth Systems*, 1(3), e220001.

Behrens, G., Beucler, T., Gentine, P., Iglesias-Suarez, F., Pritchard, M., & Eyring, V. (2022). Non-linear dimensionality reduction with a variational encoder decoder to understand convective processes in climate models. *Journal of Advances in Modeling Earth Systems*, 14(8), e2022MS003130. doi: <https://doi.org/10.1029/2022MS003130>

Bell, M. M., & Montgomery, M. T. (2019). Mesoscale processes during the genesis of hurricane karl (2010). *J. Atmos. Sci.*, 76(8), 2235–2255. doi: 10.1175/JAS-D-18-0161.1

Bu, Y. P., Fovell, R. G., & Corbosiero, K. L. (2014). Influence of cloud-radiative forcing on tropical cyclone structure. *J. Atmos. Sci.*, 71(10), 1644–1662. doi: 10.1175/JAS-D-13-0265.1

Cangialosi, J. P., Blake, E., DeMaria, M., Penny, A., Latto, A., Rappaport, E., & Tallapragada, V. (2020). Recent progress in tropical cyclone intensity forecasting at the national hurricane center. *WAF*, 35(5), 1913–1922. doi: 10.1175/WAF-D-20-0059.1

Carstens, J. D., & Wing, A. A. (2020). Tropical cyclogenesis from self-aggregated convection in numerical simulations of rotating radiative-convective equilibrium. *Journal of Advances in Modeling Earth Systems*, 12.

DeMaria, M., Sampson, C. R., Knaff, J. A., & Musgrave, K. D. (2014). Is tropical cyclone intensity guidance improving? *Bull. Amer. Meteor. Soc.*, 95, 387–398. doi: 10.1175/BAMS-D-12-00240.1

Eliassen, A. (1952). Slow thermally or frictionally controlled meridional circulations in a circular vortex. *Astrophys. Nor.*, 5, 19–60.

Fan, Y., Chung, Y. T., & Shi, X. (2021). The essential role of cloud-radiation interaction in nonrotating convective self-aggregation. *Geophys. Res. Lett.*, 48, e2021GL095102. doi: 10.1029/2021GL095102

Fischer, M. S., Tang, B. H., & Corbosiero, K. L. (2019). A climatological analysis of tropical cyclone rapid intensification in environments of upper-tropospheric trough. *Mon. Wea. Rev.*, 147(10), 3693–3719. doi:

10.1175/MWR-D-19-0013.1

Gray, W. M., & Jacobson, R. W. J. (1977). Diurnal variation of deep cumulus convection. *J. Atmos. Sci.*, *105*, 1171-1188. doi: 10.1175/1520-0493(1977)105<1171:DVODCC>2.0.CO;2

Hendricks, E. A., Montgomery, M. T., & Davis, C. A. (2004). The role of “vortical” hot towers in the formation of tropical cyclone diana (1984). *Journal of the atmospheric sciences*, *61*(11), 1209–1232.

Iacono, M. J., Delamere, J. S., Mlawer, E. J., Shephard, M. W., Clough, S. A., & Collins, W. D. (2008). Radiative forcing by long-lived greenhouse gases: Calculations with the aer radiative transfer models. *J. Geophys. Res.*, *113*(D13103). doi: 10.1029/2008JD009944

Kilroy, G. (2021). Evolution of convective characteristics during tropical cyclogenesis. *Q J R Meteorol Soc.*, *147*, 2103–2123. doi: 10.1002/qj.4011

Kingma, D. P., & Welling, M. (2022). *Auto-encoding variational bayes*.

Landsea, C. W., & Cangialosi, J. P. (2018). Have we reached the limits of predictability for tropical cyclone track forecasting? *BAMS*, *99*(11), 2237–2243. doi: 10.1175/BAMS-D-17-0136.1

Lipton, Z. C. (2018). The mythos of model interpretability: In machine learning, the concept of interpretability is both important and slippery. *Queue*, *16*(3). Retrieved from <https://doi.org/10.1145/3236386.3241340> doi: 10.1145/3236386.3241340

Mamalakis, A., Barnes, E. A., & Ebert-Uphoff, I. (2023). Carefully choose the baseline: Lessons learned from applying xai attribution methods for regression tasks in geoscience. *Artificial Intelligence for the Earth Systems*, *2*(1), e220058.

Marcinkevič, R., & Vogt, J. E. (2023). Interpretable and explainable machine learning: A methods-centric overview with concrete examples. *WIREs Data Mining and Knowledge Discovery*, *13*(3), e1493. doi: <https://doi.org/10.1002/widm.1493>

Mayer, K. J., & Barnes, E. A. (2021). Subseasonal forecasts of opportunity identified by an explainable neural network. *Geophysical Research Letters*, *48*, e2020GL092092. doi: 10.1029/2020GL092092

McGovern, A., Lagerquist, R., Gagne, D. J., Jergensen, G. E., Elmore, K. L., Homeyer, C. R., & Smith, T. (2019). Making the black box more transparent: Understanding the physical implications of machine learning. *Bulletin of the American Meteorological Society*, *100*(11), 2175–2199.

Melhauser, C., & Zhang, F. (2014). Diurnal radiation cycle impact on the pregenesis environment of hurricane karl (2010). *J. Atmos. Sci.*, *71*(4), 1241–1259. doi: 10.1175/JAS-D-13-0116.1

Muller, C., & Bony, S. (2015). What favors convective aggregation and why? *Geophys. Res. Lett.*, *42*, 5626–5634. doi: 10.1002/2015GL064260

Muller, C. J., & Romps, D. M. (2018). Acceleration of tropical cyclogenesis by self-aggregation feedbacks. *Proceedings of the National Academy of Sciences*, *115*(12), 2930–2935.

Murthy, V. S., & Boos, W. R. (2018). Role of surface enthalpy fluxes in idealized simulations of tropical depression spinup. *Journal of the Atmospheric Sciences*, *75*(6), 1811–1831. doi: 10.1175/JAS-D-17-0119.1

Nam, C. C., & Bell, M. M. (2021). Multiscale shear impacts during the genesis of hagupit (2008). *Monthly Weather Review*, *149*(2), 551–569.

Narenpitak, P., Bretherton, C. S., & Khairoutdinov, M. F. (2020). The role of multiscale interaction in tropical cyclogenesis and its predictability in near-global aquaplanet cloud-resolving simulations. *Journal of the Atmospheric Sciences*, *77*(8), 2847–2863.

Navarro, E. L., Hakim, G. J., & Willoughby, H. E. (2017). Balanced response of an axisymmetric tropical cyclone to periodic diurnal heating. *Journal of the At-*

*mospheric Sciences*, 74(10), 3325–3337.

Nicholls, M. E. (2015). An investigation of how radiation may cause accelerated rates of tropical cyclogenesis and diurnal cycles of convective activity. *Atmos. Chem. Phys.*, 15, 9003–9029. doi: 10.5194/acp-15-9003-2015

Paszke, A., Gross, S., Massa, F., Lerer, A., Bradbury, J., Chanan, G., ... Chintala, S. (2019). *Pytorch: An imperative style, high-performance deep learning library*.

Pendergrass, A. G., & Willoughby, H. E. (2009). Diabatically induced secondary flows in tropical cyclones. part i: Quasi-steady forcing. *Mon. Wea. Rev.*, 137, 805–821. doi: 10.1175/2008MWR2657.1

Ramsay, H. A. (2013). The effects of imposed stratospheric cooling on the maximum intensity of tropical cyclones in axisymmetric radiative–convective equilibrium. *J. Climate*, 26, 9977–9985. doi: 10.1175/JCLI-D-13-00195.1

Rogers, R., Reasor, P., & Lorsolo, S. (2013). Airborne doppler observations of the inner-core structural differences between intensifying and steady-state tropical cyclones. *Monthly Weather Review*, 141(9), 2970–2991.

Rogers, R. F., Reasor, P. D., Zawislak, J. A., & Nguyen, L. T. (2020). Precipitation processes and vortex alignment during the intensification of a weak tropical cyclone in moderate vertical shear. *Monthly Weather Review*, 148(5), 1899–1929.

Ruppert, J. H., & O'Neill, M. E. (2019). Diurnal cloud and circulation changes in simulated tropical cyclones. *Geophys. Res. Lett.*, 46, 502–511. doi: 10.1029/2018GL081302

Ruppert, J. H., Wing, A. A., Tang, X., & Duran, E. L. (2020). The critical role of cloud infrared radiation feedback in tropical cyclone development. *Proceedings of the National Academy of Sciences*, 117(45), 27884–27892. Retrieved from <https://www.pnas.org/doi/abs/10.1073/pnas.2013584117> doi: 10.1073/pnas.2013584117

Shimada, U., Aonashi, K., & Miyamoto, Y. (2017). Tropical cyclone intensity change and axisymmetry deduced from gsmmap. *Monthly Weather Review*, 145(3), 1003–1017.

Skamarock, W. (2008). A description of the advanced research wrf version 3. *Tech. Note*, 1–96.

Smith, W. P., Nicholls, M. E., & R. A. Pielke, S. (2020). The role of radiation in accelerating tropical cyclogenesis in idealized simulations. *J. Atmos. Sci.*, 77(4), 1261–1277. doi: 10.1175/JAS-D-19-0044.1

Tam, F. I.-H. (2024, Jan). *Trained models and data for "identifying three-dimensional radiative patterns associated with early tropical cyclone intensification"*. Zenodo. Retrieved from <http://dx.doi.org/10.5281/zenodo.10556861> doi: 10.5281/zenodo.10556861

Tang, B. H. (2017). Coupled dynamic–thermodynamic forcings during tropical cyclogenesis. part ii: Axisymmetric experiments. *J. Atmos. Sci.*, 74(7), 2279–2291. doi: 10.1175/JAS-D-17-0049.1

Thompson, G., & Eidhammer, T. (2014). A study of aerosol impacts on clouds and precipitation development in a large winter cyclone. *J. Atmos. Sci.*, 71(10), 3636–3658. doi: 10.1175/JAS-D-13-0305.1

Trabing, B. C., Bell, M. M., & Brown, B. R. (2019). Impacts of radiation and upper-tropospheric temperatures on tropical cyclone structure and intensity. *J. Atmos. Sci.*, 76(1), 135–153. doi: 10.1175/JAS-D-18-0165.1

Wang, S., Camargo, S. J., Sobel, A. H., & Polvani, L. M. (2014). Impact of the tropopause temperature on the intensity of tropical cyclones: An idealized study using a mesoscale model. *J. Atmos. Sci.*, 71, 4333–4348. doi: <https://doi.org/10.1175/JAS-D-14-0029.1>

Wang, Z. (2014). Role of cumulus congestus in tropical cyclone formation in a high-resolution numerical model simulation. *Journal of the atmospheric sciences*,

71, 1681–1700.

Willoughby, H. E. (1979). Forced secondary circulations in hurricanes. *J. Geophys. Res.*, 84(C6), 3173–3183. doi: 10.1029/JC084iC06p03173

Wing, A. A., Emanuel, K., Holloway, C., & Muller, C. (2017). Convective self-aggregation in numerical simulations: A review. *Surv Geophys*, 38, 1173–1197. doi: 10.1007/s10712-017-9408-4

Wing, A. A., & Emanuel, K. A. (2014). Physical mechanisms controlling self-aggregation of convection in idealized numerical modeling simulations. *J. Adv. Model. Earth. Syst.*, 6, 59–74. doi: 10.1002/2013MS000269

Wu, S.-N., Soden, B. J., & Nolan, D. S. (2021). Examining the role of cloud radiative interactions in tropical cyclone development using satellite measurements and wrf simulations. *Geophys. Res. Lett.*, 48, e2021GL093259. doi: 10.1029/2021GL093259

Xu, W., Rutledge, S. A., & Zhang, W. (2017). Relationships between total lightning, deep convection, and tropical cyclone intensity change. *Journal of Geophysical Research: Atmospheres*, 122(13), 7047–7063.

Yang, B., & Tan, Z. (2018). Interactive radiation accelerates the intensification of the midlevel vortex for tropical cyclogenesis. *Journal of the Atmospheric Sciences*, 77(12), 4051–4065. doi: 10.1175/JAS-D-20-0094.1

Zagrodnik, J. P., & Jiang, H. (2014). Rainfall, convection, and latent heating distributions in rapidly intensifying tropical cyclones. *Journal of the Atmospheric Sciences*, 71(8), 2789–2809.

Zhang, F., & Emanuel, K. (2016). On the role of surface fluxes and wishe in tropical cyclone intensification. *Journal of the Atmospheric Sciences*, 73(5), 2011–2019. doi: 10.1175/JAS-D-16-0011.1

# Supporting Information for

## Identifying Three-Dimensional Radiative Patterns Associated with Early Tropical Cyclone Intensification

Frederick Iat-Hin Tam, Tom Beucler, James H. Ruppert Jr.

Frederick Iat-Hin Tam  
E-mail: ft21894@gmail.com

### This PDF file includes:

Supporting text  
Figs. S1 to S6  
Tables S1 to S3  
SI References

## Supporting Information Text

### 1. Details of the Machine Learning Framework

The proposed interpretable machine learning model consists of three parts: (i) a dimensionality reduction layer to process full complexity input fields in physical units, (ii) a linear encoder that condenses all low-dimensionality representations of a physical field into a projection that is most useful to the prediction task, and (iii) a final linear decoder that uses multiple linear regression to give the 24-hour TC intensification rates based on a given set of input fields.

**A. Mathematical Construction.** This section presents full mathematical descriptions of the three different parts of the ML framework.

We choose to use Principal Component Analysis (PCA) to preserve linearity in the dimensionality reduction layer. PCA linearly transforms input physical fields ( $X_i$ ) into combinations of orthogonal eigenvectors (PCA modes;  $\Pi_{X_i}(z, r, \theta)$ ) and their corresponding time evolution (PC loadings time series;  $PC_{X_i}(t)$ ):

$$X_i(t, z, r, \theta) - \overline{X_i(t, z, r, \theta)} = \sum_{i=1}^N PC_{X_i}(t) \Pi_{X_i}(z, r, \theta), \quad [1]$$

where  $N$  is the number of retained PCA modes. Different loadings  $PC_{X_i}(t)$  given by the PCA will be used as inputs to the ML model, instead of the raw field  $X_i$  in its full spatiotemporal complexity.

Following best machine learning practices, all  $PC_{X_i}(t)$  time series are standardized to have a mean of 0 and a variance of 1 to avoid high variance in the regression weights:

$$\widetilde{PC}_{X_i}(t) = \frac{PC_{X_i}(t) - \overline{PC_{X_i}(t)}}{\sigma_{PC_{X_i}(t)}}, \quad [2]$$

where  $\overline{PC_{X_i}}$  and  $\sigma_{PC_{X_i}(t)}$  are the mean and standard deviation of the PC loadings, calculated over the training set.

In the encoder module of our VED model, we combine different PCA modes for longwave radiation and shortwave radiation into two “mean structures” ( $\Pi_{LW,\mu}$ ,  $\Pi_{SW,\mu}$ ) and two “logarithmic variance structures” ( $\Pi_{LW,\log\sigma^2}$ ,  $\Pi_{SW,\log\sigma^2}$ ). These data-driven structures do not vary in time. The model’s first layer involves projecting the original radiation fields onto the learned mean and logarithmic variance structures. We now introduce an inner product that will help us define this projection:

$$\langle PC_{X_1} | PC_{X_2} \rangle_{X_3} = \sum_{i=1}^N PC_{X_1}^i PC_{X_2}^i, \quad [3]$$

the  $X_3$  indicates that the inner product and the projection are defined with respect to the variable for which the PC decomposition and orthogonal modes are calculated.

Using this notation, the 24-hr surface intensity intensification rates may be computed with the projections obtained in the first model layer:

$$\begin{aligned} \left( \frac{dV_{surf}}{dt} \right)_{24hr} &= a_{LW} \mathcal{N} \left( \langle LW | \Pi_{\mu LW} \rangle_{LW}, c_{LW} e^{d_{LW} \langle LW | \Pi_{\log \sigma^2_{LW}} \rangle_{LW}} \right) \\ &+ a_{SW} \mathcal{N} \left( \langle SW | \Pi_{\mu SW} \rangle_{SW}, c_{SW} e^{d_{SW} \langle SW | \Pi_{\log \sigma^2_{SW}} \rangle_{SW}} \right) \\ &+ b, \end{aligned} \quad [4]$$

where the input of the final linear decoder is given by randomly sampling the normal distributions constructed with the mean and logarithmic variances calculated by the linear encoder for longwave and shortwave radiation. We will show that the “effective weight” to calculate the contribution of longwave radiation (in physical units) to TC intensification can be expressed by:

$$a_{LW} = |a_{2,LW}| \sqrt{\sum_{i=1}^{n_{LW}} \frac{a_{1,LW,\mu,i}^2}{\sigma (PC_{i,LW})^2}}, \quad [5]$$

whereas the weight of the shortwave contribution is

$$a_{SW} = |a_{2,SW}| \sqrt{\sum_{i=1}^{n_{SW}} \frac{a_{1,SW,\mu,i}^2}{\sigma (PC_{i,SW})^2}}. \quad [6]$$

We will also show that the overall model bias ( $b$ ) is given by the following equation:

$$b = b_2 + a_{2,LW} \left( b_{1,LW,\mu} - \sum_{i=1}^{n_{LW}} \frac{a_{1,LW,\mu,i} \overline{PC}_{i,LW}}{\sigma( \overline{PC}_{i,LW})} \right) + a_{2,SW} \left( b_{1,SW,\mu} - \sum_{i=1}^{n_{SW}} \frac{a_{1,SW,\mu,i} \overline{PC}_{i,SW}}{\sigma( \overline{PC}_{i,SW})} \right), \quad [7]$$

and that the four constants involved in the variance calculation ( $c_{LW}, c_{SW}, d_{LW}, d_{SW}$ ) are given by the following equations:

$$c_{LW} = \left( \sum_{i=1}^{n_{LW}} \frac{a_{1,LW,\mu,i}^2}{\sigma( \overline{PC}_{i,LW})^2} \right)^{-1/4} \exp \left( b_{1,LW,\log \sigma^2} - \sum_{i=1}^{n_{LW}} a_{1,LW,\log \sigma^2,i} \frac{\overline{PC}_{i,LW}}{\sigma( \overline{PC}_{i,LW})} \right), \quad [8]$$

$$c_{SW} = \left( \sum_{i=1}^{n_{SW}} \frac{a_{1,SW,\mu,i}^2}{\sigma( \overline{PC}_{i,SW})^2} \right)^{-1/4} \exp \left( b_{1,SW,\log \sigma^2} - \sum_{i=1}^{n_{SW}} a_{1,SW,\log \sigma^2,i} \frac{\overline{PC}_{i,SW}}{\sigma( \overline{PC}_{i,SW})} \right), \quad [9]$$

$$d_{LW} = \sqrt{\sum_{i=1}^{n_{LW}} \frac{a_{1,LW,\log \sigma^2,i}^2}{\sigma( \overline{PC}_{i,LW})^2}}, \quad [10]$$

$$d_{SW} = \sqrt{\sum_{i=1}^{n_{SW}} \frac{a_{1,SW,\log \sigma^2,i}^2}{\sigma( \overline{PC}_{i,SW})^2}}. \quad [11]$$

The parameters  $b_2$ ,  $a_{2,LW}$ , and  $a_{2,SW}$  represent the bias term, weights for longwave radiation, and the weights for shortwave radiation in the final regression layer, respectively. The constants also includes the weights and biases from the longwave mean structure encoder ( $a_{1,LW,\mu}$ ,  $b_{1,LW,\mu}$ ), the shortwave mean structure encoder ( $a_{1,SW,\mu}$ ,  $b_{1,SW,\mu}$ ), the temporal average of PC time series ( $\overline{PC}_{i,LW}$ ,  $\overline{PC}_{i,SW}$ ), and their standard deviations ( $\sigma( \overline{PC}_{i,LW})$ ,  $\sigma( \overline{PC}_{i,SW})$ ). Using this notation, the four outputs of our model's first (projection) layer are given by the following four equations:

$$\begin{aligned} \mu_{LW} &= b_{1,LW,\mu} + \sum_{i=1}^{n_{LW}} a_{1,LW,\mu,i} \times \widetilde{PC}_{i,LW}, \\ \log \sigma_{LW}^2 &= b_{1,LW,\log \sigma^2} + \sum_{i=1}^{n_{LW}} a_{1,LW,\log \sigma^2,i} \times \widetilde{PC}_{i,LW}, \\ \mu_{SW} &= b_{1,SW,\mu} + \sum_{i=1}^{n_{SW}} a_{1,SW,\mu,i} \times \widetilde{PC}_{i,SW}, \\ \log \sigma_{SW}^2 &= b_{1,SW,\log \sigma^2} + \sum_{i=1}^{n_{SW}} a_{1,SW,\log \sigma^2,i} \times \widetilde{PC}_{i,SW}, \end{aligned} \quad [12]$$

and the output of our model's second (prediction) layer is given by the following equation:

$$\begin{aligned} \left( \frac{dV_{surf}}{dt} \right)_{24hr} &= a_{2,LW} \mathcal{N} \left( \mu_{LW}, e^{\log \sigma_{LW}^2} \right) \\ &+ a_{2,SW} \mathcal{N} \left( \mu_{SW}, e^{\log \sigma_{SW}^2} \right) \\ &+ b_2. \end{aligned} \quad [13]$$

Combining equations 2, 12, and 13 yields:

$$\begin{aligned} \left( \frac{dV_{surf}}{dt} \right)_{24hr} &= a_{2,LW} \mathcal{N} \left( \sum_{i=1}^{n_{LW}} \frac{a_{1,LW,\mu,i}}{\sigma( \overline{PC}_{i,LW})} \overline{PC}_{i,LW}, e^{\log \sigma_{LW}^2} \right) \\ &+ a_{2,SW} \mathcal{N} \left( \sum_{i=1}^{n_{SW}} \frac{a_{1,SW,\mu,i}}{\sigma( \overline{PC}_{i,SW})} \overline{PC}_{i,SW}, e^{\log \sigma_{SW}^2} \right) \\ &+ b. \end{aligned} \quad [14]$$

We can rewrite Equation 14 to include the prefactors  $a_{2,LW}$  and  $a_{2,SW}$  in the mean and variances of the two normal distributions used to calculate the intensification rate:

$$\begin{aligned} \left( \frac{dV_{surf}}{dt} \right)_{24hr} &= \mathcal{N} \left( \sum_{i=1}^{n_{LW}} \frac{a_{2,LW} a_{1,LW,\mu,i}}{\sigma(PC_{i,LW})} PC_{i,LW}, \sqrt{a_{2,LW}} e^{\log \sigma_{LW}^2} \right) \\ &+ \mathcal{N} \left( \sum_{i=1}^{n_{LW}} \frac{a_{2,SW} a_{1,SW,\mu,i}}{\sigma(PC_{i,SW})} PC_{i,SW}, \sqrt{a_{2,SW}} e^{\log \sigma_{SW}^2} \right) \\ &+ b. \end{aligned} \quad [15]$$

We can now use the definition of the inner product (Eq 3) to interpret our model's first layer as a linear projection onto four data-driven structures:  $(\Pi_{\mu LW}, \Pi_{\mu SW}, \Pi_{\log \sigma^2 LW}, \Pi_{\log \sigma^2 SW})$ . According to the inner product's definition (given by Equation 3), the PC loadings  $(PC_{i,\Pi_{\mu LW}}, PC_{i,\Pi_{\mu SW}}, PC_{i,\Pi_{\log \sigma^2 LW}}, PC_{i,\Pi_{\log \sigma^2 SW}})$  of these four structures obey the following equations:

$$\begin{cases} \langle LW | \Pi_{\mu LW} \rangle_{LW} &= \sum_{i=1}^{n_{LW}} PC_{i,LW} \times PC_{i,\Pi_{\mu LW}}, \\ \langle LW | \Pi_{\log \sigma^2 LW} \rangle_{LW} &= \sum_{i=1}^{n_{LW}} PC_{i,LW} \times PC_{i,\Pi_{\log \sigma^2 LW}}, \\ \langle SW | \Pi_{\mu SW} \rangle_{SW} &= \sum_{i=1}^{n_{LW}} PC_{i,SW} \times PC_{i,\Pi_{\mu SW}}, \\ \langle SW | \Pi_{\log \sigma^2 SW} \rangle_{SW} &= \sum_{i=1}^{n_{LW}} PC_{i,SW} \times PC_{i,\Pi_{\log \sigma^2 SW}}. \end{cases} \quad [16]$$

Substituting Equation 15 into Equation 4 and building upon the equivalence of equations 4 and 14, we see that the PC loadings of the longwave mean structure  $PC_{i,\Pi_{\mu LW}}$  are proportional to the product of the first two layers' weights:

$$PC_{i,\Pi_{\mu LW}} = \lambda \frac{a_{2,LW} a_{1,LW,\mu,i}}{\sigma(PC_{i,LW})}, \quad [17]$$

where we have used  $\lambda$  to denote the proportionality coefficient in the case of the longwave "mean structure". To simplify the projection's definition, the norm of the data-driven structure is assumed to be 1:

$$1 = \langle \Pi_{\mu LW} | \Pi_{\mu LW} \rangle_{LW} = \sum_{i=1}^{n_{LW}} PC_{i,\Pi_{\mu LW}}^2 = \lambda^2 a_{2,LW}^2 \sum_{i=1}^{n_{LW}} \frac{a_{1,LW,\mu,i}^2}{\sigma(PC_{i,LW})^2} \quad [18]$$

This means that the proportionality coefficient  $\lambda$  in Equation (17) is:

$$\lambda = \left[ |a_{2,LW}| \sqrt{\sum_{i=1}^{n_{LW}} \frac{a_{1,LW,\mu,i}^2}{\sigma(PC_{i,LW})^2}} \right]^{-1}. \quad [19]$$

Substituting Equation (19) into Equation (14) and taking the definition of the inner products (Eq. 3) into account, we obtain:

$$\begin{aligned} \left( \frac{dV_{surf}}{dt} \right)_{24hr} &= \mathcal{N} \left( \sqrt{\sum_{i=1}^{n_{LW}} \frac{a_{1,LW,\mu,i}^2}{\sigma(PC_{i,LW})^2}} \underbrace{\frac{a_{2,LW}}{\text{sign}(a_{2,LW})} \sum_{i=1}^{n_{LW}} PC_{i,\Pi_{\mu LW}} PC_{i,LW}}_{|a_{2,LW}| \langle LW | \Pi_{\mu LW} \rangle}, \sqrt{a_{2,LW}} e^{\log \sigma_{LW}^2} \right) \\ &+ \mathcal{N} \left( \sqrt{\sum_{i=1}^{n_{SW}} \frac{a_{1,SW,\mu,i}^2}{\sigma(PC_{i,SW})^2}} \underbrace{\frac{a_{2,SW}}{\text{sign}(a_{2,SW})} \sum_{i=1}^{n_{SW}} PC_{i,\Pi_{\mu SW}} PC_{i,SW}}_{|a_{2,SW}| \langle SW | \Pi_{\mu SW} \rangle}, \sqrt{a_{2,SW}} e^{\log \sigma_{SW}^2} \right) \\ &+ b \end{aligned} \quad [20]$$

To see how Equation 20 related to Equation (4), we factor out all constant terms from the normal distribution:

$$\begin{aligned} \left( \frac{dV_{surf}}{dt} \right)_{24hr} &= \underbrace{|a_{2,LW}| \sqrt{\sum_{i=1}^{n_{LW}} \frac{a_{1,LW,\mu,i}^2}{\sigma (PC_{i,LW})^2}}}_{a_{LW}} \mathcal{N} \left( \langle LW | \Pi_{\mu LW} \rangle_{LW}, \frac{e^{\log \sigma_{LW}^2}}{\left( \sum_{i=1}^{n_{LW}} \frac{a_{1,LW,\mu,i}^2}{\sigma (PC_{i,LW})^2} \right)^{1/4}} \right) \\ &+ \underbrace{|a_{2,SW}| \sqrt{\sum_{i=1}^{n_{SW}} \frac{a_{1,SW,\mu,i}^2}{\sigma (PC_{i,SW})^2}}}_{a_{SW}} \mathcal{N} \left( \langle SW | \Pi_{\mu SW} \rangle_{SW}, \frac{e^{\log \sigma_{SW}^2}}{\left( \sum_{i=1}^{n_{SW}} \frac{a_{1,SW,\mu,i}^2}{\sigma (PC_{i,SW})^2} \right)^{1/4}} \right) \\ &+ b, \end{aligned} \quad [21]$$

allowing us to identify the “effective weights”  $a_{LW}$  and  $a_{SW}$ . We now use the definition of the logarithmic variance in the model’s first (projection) layer (12) to expand the logarithmic variance term of the normal distributions:

$$\begin{aligned} \left( \frac{dV_{surf}}{dt} \right)_{24hr} &= a_{LW} \mathcal{N} \left( \langle LW | \Pi_{\mu LW} \rangle_{LW}, \frac{b_{1,LW,\log \sigma^2} + \sum_{i=1}^{n_{LW}} a_{1,LW,\log \sigma^2,i} \times \widetilde{PC}_{i,LW}}{\left( \sum_{i=1}^{n_{LW}} \frac{a_{1,LW,\mu,i}^2}{\sigma (PC_{i,LW})^2} \right)^{1/4}} \right) \\ &+ a_{SW} \mathcal{N} \left( \langle SW | \Pi_{\mu SW} \rangle_{SW}, \frac{b_{1,SW,\log \sigma^2} + \sum_{i=1}^{n_{SW}} a_{1,SW,\log \sigma^2,i} \times \widetilde{PC}_{i,SW}}{\left( \sum_{i=1}^{n_{SW}} \frac{a_{1,SW,\mu,i}^2}{\sigma (PC_{i,SW})^2} \right)^{1/4}} \right) \\ &+ b \end{aligned} \quad [22]$$

We notice that parts of Equation 22 are constant, which means that we can simplify this equation further by defining variance prefactors for longwave radiation ( $c_{LW}$ ; Eq. 8) and shortwave radiation ( $c_{SW}$ ; Eq. 9). The standard deviation terms in the normal distributions can now be written in a simpler format:

$$\frac{\exp \left( b_{1,LW,\log \sigma^2} + \sum_{i=1}^{n_{LW}} a_{1,LW,\log \sigma^2,i} \times \widetilde{PC}_{i,LW} \right)}{\left( \sum_{i=1}^{n_{LW}} \frac{a_{1,LW,\mu,i}^2}{\sigma (PC_{i,LW})^2} \right)^{1/4}} = c_{LW} \exp \left( \underbrace{\sqrt{\sum_{i=1}^{n_{LW}} \frac{a_{1,LW,\log \sigma^2,i}^2}{\sigma (PC_{i,LW})^2}}}_{d_{LW}} \times \left\langle LW \mid \Pi_{\log \sigma_{LW}^2} \right\rangle_{LW} \right), \quad [23]$$

$$\frac{\exp \left( b_{1,SW,\log \sigma^2} + \sum_{i=1}^{n_{SW}} a_{1,SW,\log \sigma^2,i} \times \widetilde{PC}_{i,SW} \right)}{\left( \sum_{i=1}^{n_{SW}} \frac{a_{1,SW,\mu,i}^2}{\sigma (PC_{i,SW})^2} \right)^{1/4}} = c_{SW} \exp \left( \underbrace{\sqrt{\sum_{i=1}^{n_{SW}} \frac{a_{1,SW,\log \sigma^2,i}^2}{\sigma (PC_{i,SW})^2}}}_{d_{SW}} \times \left\langle SW \mid \Pi_{\log \sigma_{SW}^2} \right\rangle_{SW} \right). \quad [24]$$

Using the same reasoning as for the mean data-driven structure, we find the proportionality coefficient ( $\nu$ ) for the PC loadings of the logarithmic variance structure:

$$PC_{i,\Pi \log \sigma_{LW}^2} = \nu \frac{a_{1,LW,\log \sigma^2,i}}{\sigma (PC_{i,LW})} \Rightarrow \nu = \left( \sum_{i=1}^{n_{LW}} \frac{a_{1,LW,\log \sigma^2,i}^2}{\sigma (PC_{i,LW})^2} \right)^{-1/2}. \quad [25]$$

We can now express the logarithmic variance structure’s PC loadings as:

$$PC_{\Pi \log \sigma_{LW}^2} = \left( \sum_{i=1}^{n_{LW}} \frac{a_{1,LW,\log \sigma^2,i}^2}{\sigma (PC_{i,LW})^2} \right)^{-1/2} \frac{a_{1,LW,\log \sigma^2,i}}{\sigma (PC_{i,LW})}. \quad [26]$$

For consistency with the mean structures, we transform the logarithmic variance term (Eq. 23-24) using the inner product definition:

$$c_{LW} \exp \left( \sum_{i=1}^{n_{LW}} \frac{a_{1,LW, \log \sigma^2, i} \times PC_{i,LW}}{\sigma (PC_{i,LW})} \right) = c_{LW} \exp \left( \underbrace{\sqrt{\sum_{i=1}^{n_{LW}} \frac{a_{1,LW, \log \sigma^2, i}^2}{\sigma (PC_{i,LW})^2}} \times \left\langle LW \mid \Pi_{\log \sigma^2_{LW}} \right\rangle_{LW}}_{d_{LW}} \right) \quad [27]$$

Using this simplification, we derive Equation 4 in the SI, which is equivalent to Equation 1 in the main text. We will now elaborate upon the short description in the main text on several important aspects of the model training procedure. Specifically, we discuss the cross-validation strategy, hyperparameter settings, and the overall workflow used to train the VED models.

**B. Cross-validation strategy.** We train multiple models on different cross-validation splits to evaluate the sensitivity of model prediction skills to what ensemble members or sensitivity experiments are included in the training data and ensure the trained models are generalizable to out-of-sample data. Since ensemble simulations and sensitivity experiments can be treated as different realizations of the same physical system responding to slightly different forcing, we opt for a data-splitting strategy based on ensemble member labels.

For Haiyan, 80% of the ensemble outputs (16 experiments) are used for training, and 20% of the data (4 experiments) is left for validation and testing. We create different splits by first choosing two experiments as an independent test set; the remaining 18 experiments are partitioned into training and validation subsets by randomly generating a list of two numbers between 1 and 20; the two numbers are then used as references to separate the validation set from the training set. This data-splitting procedure is repeated forty times to fully sample the model variability associated with the choice of data split. To avoid information leakage to the trained models, the test set is truly independent in that the two experiments in it are never used in the training or validation set in all 40 splits. The reference list to create and produce our dataset is shown in Table S3.

For Maria, we slightly altered the data-splitting strategy due to a lack of samples. The Control (CTRL) simulation is always included in the training set because it has the most samples and represents how the TC evolves in realistic conditions where CRF always exists. The NCRF36 experiment is used as the test dataset amongst the four remaining sensitivity experiments because the storm intensity changes in that experiment depart most from the CTRL simulation. The other experiments are randomly split into a portion that would be merged into the training set (2 experiments) and the other portion for model validation (1 experiment). The cross-validation strategy for Maria yields three different data splits to test the ability of the trained ML models to depict the counterfactual of TC evolution without cloud radiative feedback (CRF).

**C. Hyperparameter settings and model optimization.** Next, we describe the hyperparameter settings and how they are tuned to create one probabilistic ML model. All models presented herein are implemented and trained with the PyTorch deep learning library (1). The Adam Optimizer is used to perform stochastic gradient descent for all trained models. The Optuna hyperparameter tuning framework (2) is used to find the best set of hyperparameters for one particular data split. In the VED framework, there are two main hyperparameters to optimize - the learning rate, which determines the step at which the SGD optimization process proceeds, and the VED loss coefficient. The VED architecture requires a specialized loss function for optimization. The loss function used in this study is defined as follows:

$$\text{VEDloss} = \nu \text{Reconstruction Loss} + (1 - \nu) \text{KLloss}, \quad [28]$$

where  $\nu \in [0, 1]$  is the weight of the reconstruction loss in the overall VED loss. The role of  $\nu$  will be expanded upon in the subsequent paragraphs. The objective of the encoder module in the VED architecture can be formulated as finding the posterior probability of latent representation  $Z$  given input  $X$  ( $p(Z|X)$ ). From Bayes' theorem:

$$p(Z|X) = \frac{p(X|Z)p(Z)}{p(X)} \quad [29]$$

This posterior is difficult to calculate due to the intractable  $p(X)$  term. The VED model solves this problem by having a parameterized prior. We want to make the learned data distribution as close to the prior as possible for regularization. The VED loss implemented in the model can be treated as combining the usual loss function objective for the decoding regression module (the “reconstruction loss” in Eq. 28; MAE in this case) and an extra KL regularization term that forces the latent data representation distributions to be close to the prior. The KL regularization term accomplishes the objective of approximating the true conditional probability term  $p(X|Z)$  using the predefined prior. Mathematically, this is equivalent to minimizing the Kullback-Leibler (KL) divergence between the prior and the true conditional probability term  $p(X|Z)$ . By using the “reparameterization trick” (3), the KL loss implemented in this model can be expressed as:

$$\text{KLloss} = \frac{1}{2} \times \frac{1}{N} \sum_{j=1}^N \sum_{k=1}^K \left[ -1 - \ln \sigma_{jk}^2 + \mu_{jk}^2 + \sigma_{jk}^2 \right], \quad [30]$$

where  $N$  equals batch size, and  $K$  represents the width of the latent space. The mean and variance of the learned Gaussian distribution are represented by  $\mu$  and  $\sigma$ . We calculate the  $\mu$  and  $\sigma$  for every batch ( $j$ ) and latent dimension ( $k$ ) of the training data. Minimizing the summation of these terms ensures that the learned data distribution is close to the prior after training.

For every cross-validation fold, a set of best hyperparameters minimizing training VAE loss is saved. The main hyperparameter to tune in our model is the learning rate. For a given hyperparameter set, seven trials are conducted to account for stochasticity associated with weight initialization. The KL term can result in the model finding a latent representation too close to the uninformative Gaussian prior - a phenomenon known as posterior collapse (4). A KL annealing approach is used to optimize the VED model to avoid this phenomenon. A summary of the KL annealing approach is to train the VED model without KL loss for a certain time and focus on optimizing the decoder prediction task. We continue to train the partially trained model with different strengths of the KL loss by making the  $\nu$  coefficient less than 1. We tune  $\nu$  manually and save all models with different  $\nu$  instead of optimizing it automatically with Optuna because we wanted to show the full sensitivity of model performance to  $\nu$ . When initializing the optimizer, all parameters are set to default values in PyTorch, with the only exception being the learning rate. Other optimizers are tested, but they did not perform satisfactorily on the prediction task. 280 VED models were trained and stored for the Haiyan ensemble experiments, whereas 21 models were trained for the Maria experiments.

**D. Evaluating the trained probabilistic models.** The trained VED models are evaluated with two criteria - good mean prediction skills and a well-calibrated uncertainty in the model outputs. We sample the model spread by running each model 30 times and comparing the 30 model predictions. A suite of stochastic and determinative performance metrics are used to assess the quality of the model. Two stochastic metrics are evaluated: the CRPS score and the SSREL value (5).

The CRPS score compares the Cumulative Distribution Function (CDF) of the probabilistic forecasts against the observations; it is also a generalization of the deterministic mean absolute error (MAE) metric for probabilistic models:

$$\text{CRPS}(F, y_{true}) = \int_{-\infty}^{\infty} [F(y_{pred}) - \mathcal{H}(y_{pred} - y_{true})]^2 dy_{pred}, \quad [31]$$

where  $F$  represents the CDF of the model predictions,  $\mathcal{H}$  is the Heaviside step function applied to the difference between the truth ( $y_{true}$ ) and one prediction ( $y_{pred}$ ) sampled from the full distribution. By definition, the Heaviside function outputs 1 if the prediction is larger than the truth and 0 in the opposite case. A well-calibrated model should have as small a CRPS score as possible.

The SSREL value (5) measures the quality of a binned spread-skill plot. The binned spread-skill plot is an assessment of the statistical consistency of a probabilistic model (6). Statistical consistency refers to the situation where the probabilistic model likely samples from the same underlying distribution as that in the truth. A statistically consistent model should have its spread closely match its error. If the spread-skill curve of a model deviates from the 1-1 line in a binned spread-skill plot, the model is either under-dispersive (overconfident) or over-dispersive (underconfident), both being undesirable traits of a probabilistic prediction model. The SSREL value measures weighted distances between the model curve and the 1-1 line:

$$\text{SSREL} = \sum_{k=1}^K \frac{N_k}{N} [\text{RMSE}_k - \overline{\text{SD}}_k], \quad [32]$$

where  $K$  is the number of bins,  $N_k$  is the number of samples in a bin,  $N$  is the total number of samples,  $\text{RMSE}_k$  is the root-mean-square-error of the model predictions for samples within the bin,  $\text{SD}$  is the standard deviation of the model predictions.

A perfectly calibrated model will have a model curve that overlaps the 1-1 line, which corresponds to an SSREL value of 0. We report two metrics for the mean deterministic skills: the mean absolute error (MAE) and root mean squared error (RMSE).

**E. Model baseline.** We implement a simple two-layer linear regression model (Fig. S1) as a baseline to examine if the more complex VED architecture improves the overall prediction skills and provides a more well-calibrated prediction uncertainty. This baseline is analogous to a two-branch principal component regression. We opt for optimizing it through stochastic gradient descent to enhance flexibility in selecting the loss function, in this case, Mean Absolute Error (MAE).

Compared to the linear VED case, the baseline model only extracts two structures from the longwave and shortwave radiation information. These structures are analogous to the  $\mu_{LW}$  and  $\mu_{SW}$  in the VED model. Rather than extracting the uncertainty structures and sampling them with the reparameterization trick, we introduce uncertainty in the baseline model by using a dropout mechanism. The dropout mechanism zeroes out a random selection of input sections, which allows the model to have uncertainties in both the structure layer level and the final prediction outputs. Dropout layers are added to both channels in the first structure extraction layer and the final prediction layer, allowing the quantification of uncertainties in the structures and the predictions. The amount of input features dropped by this operation is determined by the **dropout rate** hyperparameter, a hyperparameter that ranges from 0 to 1. Larger **dropout rate** values mean more input features are kept during inference, and vice versa.

**F. Choosing the best VED model and comparison with the best baseline model.** Here, we describe the strategy to choose the best model to produce the results shown in the main text. The best model is chosen objectively based on the stochastic metrics discussed in the previous section. Figure S2 shows the minimum and median CRPS scores for all trained Haiyan VED and baseline models with different hyperparameters on the validation set. This figure allows us to compare the models with discern

the sensitivity of model skills towards critical hyperparameters related to stochasticity - the **dropout rate** for the baseline models, and the VED loss coefficient ( $\lambda$ ) for the VED models. We also substitute the fully linear prediction layer in the baseline model with feed-forward neural networks for different depths to evaluate if adding nonlinearity to the models improves the prediction skills.

Adding nonlinearity degrades the median CRPS scores for all models for most **dropout rates** (Fig. S2,S4), which justifies keeping the model fully linear. The reason why a fully linear model is sufficient here is likely due to the low sample regime situation we have for this particular problem. The median CRPS score curves for all baseline models (Fig. S2,S4) are parabola-shaped, with distinct minima, suggesting the existence of an optimal range of **dropout rates** that is desirable for better model generalizability.

We now turn our focus to the VED models. Adding the median VED CRPS scores for all trained VED models with different  $\lambda$  shows deteriorated prediction skills for a  $\lambda$  that is too small, i.e., too large a KL loss during training. The CRPS values for the minimum VED model with a given  $\lambda$  show that the best model is created when  $\lambda$  equals 0.85.

The CRPS score comparison above establishes optimal values for the **dropout rates** (the baseline models) and  $\lambda$  (the VED models). The best models for comparison are determined by calculating the SSREL scores for all models trained with the optimal coefficients.

The spread-skill plot for the best baseline and VED models (Fig. S3) provides a strong justification for using the VED model in our study. Specifically, the spread-skill curve of the VED model is much shorter than the baseline one, which indicates the VED predictions are more accurate. Plotting the full predictions of the best VED and baseline model shows that the VED better captures the peaks in the training dataset. The VED model also removes the large biases in early intensification rates seen in the baseline predictions on the test set. The VED curve is much closer to the 1-1 line than the baseline model curve. Based on these comparisons, we conclude that the VED model is superior to the baseline model for our research task because it makes smaller prediction errors and has better-calibrated uncertainty.

For Maria, the best VED model performs similarly to the best baseline model in terms of the minimum CRPS score (Fig. S4). The uncertainty for both the best baseline model and best VED model are well calibrated. However, the VED model is again preferable for Maria because of the smaller prediction errors (Fig. S5).

Interestingly, the benefit of the VED model compared to the baseline model seems to scale to the sample size. The VED model always overperforms the baseline for the Haiyan ensemble case with a larger sample size (Table S1), whereas the VED model mostly only overperforms the baseline in probabilistic metrics for the Maria simulations (Table S2).

## 2. Scientific Interpretation with the Machine Learning Framework

This section complements Section 4 in the main text and elaborates on the procedure we took to get some key physical interpretations with our machine learning model. Specifically, we rely on the fully linear nature of the ML framework discussed in Section A. This allows us to design targeted sensitivity analysis to address specific scientific problems.

**A. Decomposition by Vertical Levels.** This section provides support for the statement in the main text that “shallow cloud contribution to intensification is between two times and one order of magnitude smaller than the upper-level radiative contribution”. For this purpose, we discuss the scientific framing, preprocessing of data, and the relevant sensitivity experiment results.

**Methodology** We isolate the effect of heating anomalies in different vertical levels by zeroing out all grid point values in the input data *except grid points at the interested vertical level*. Projecting the perturbed inputs on the PC eigenvectors gives a new set of PC coefficients that the ML model can use. The model predictions with the new PC inputs represent the contribution radiation at the interested vertical level has on the overall intensification forecast. In other words, we frame these sensitivity experiments as a linear decomposition problem.

Taking longwave radiation as an example, we can separate the LW field into three separate terms:

$$LW = LW_{100} + LW_{1000} + LW_{200-900}, \quad [33]$$

where  $LW_{100}$  ( $LW_{1000}$ ) is the longwave field where all grid points except those at 100 (1000) hPa are zeroed out,  $LW_{200-900}$  is the longwave field where grid points at 100 and 1000 hPa are zeroed out.

Projecting the three components of the right hand side of Eq. 33 onto the longwave PC eigenvectors yields the same decomposition for the PC loadings:

$$\forall i \in [1, n_{LW}], PC_{i,LW} = PC_{i,LW_{100}} + PC_{i,LW_{1000}} + PC_{i,LW_{200-900}} \quad [34]$$

After standardization, Equation (34) can be separated into a constant part:

$$\underbrace{\left( \frac{\overline{PC_{i,LW_{100}}} + \overline{PC_{i,LW_{1000}}} + \overline{PC_{i,LW_{200-900}}}}{\sigma(PC_{i,LW})} \right)}_{\overline{PC_{i,LW}}} \quad [35]$$

and a part that varies in time:

$$\underbrace{\left[ \frac{PC_{i,LW100}}{\sigma(PC_{i,LW})} + \frac{PC_{i,LW1000}}{\sigma(PC_{i,LW})} + \frac{PC_{i,LW900-200}}{\sigma(PC_{i,LW})} \right]}_{PC_{i,LW}}, \quad [36]$$

Substituting Equation 36 into Equation 15 and expanding the first term in Equation 15, we can decompose surface intensification into additive terms that match the longwave radiative heating field's decomposition of Eq. 33.

$$\begin{aligned} \frac{dV_{surf,24}}{dt} = & \left( \frac{dV_{LW,100hPa}}{dt} + \frac{dV_{LW,200-1000hPa}}{dt} \right) \\ & + \frac{dV_{SW,100-1000hPa}}{dt} + b, \end{aligned} \quad [37]$$

where  $\frac{dV_{LW,100hPa}}{dt}$  quantifies how radiation anomalies at 100 hPa affect the surface intensification.

**Result** A key interpretation of this paper relies on identifying a suitable vertical level where radiation likely yields the most effect on TC genesis. Decomposing the predictions into different components allows us to quantify their relative impacts. Here, we define radiation anomaly at 100 hPa as a proxy for the deep convection radiation effect and 1000 hPa as a proxy for the shallow cloud radiation. Figure S6, which compares the decomposed longwave contributions at two vertical levels, shows the intensification associated with upper-level radiation to consistently be larger than the intensification associated with the radiative anomalies at 1000 hPa. This is true across all Haiyan ensemble members and almost all periods during the TC life cycle. This result leads us to focus mostly on the upper-level radiative anomalies when we interpret the extracted structures. Note that our model's structure does not allow us to find a direct causal link between the shallow cloud radiative feedback, deep convective cloud radiation, and surface wind intensification.

### 3. Frozen Moist Static Energy Variance Budget

The Frozen Moist Static Energy Spatial Variance Budget used in the main text follows the approach of (7). Frozen Moist Static Energy ( $h$ ), a variable conserved during moist adiabatic processes, can be expressed as:

$$h = C_p T + gz + L_v q_v - L_f q_{ice}, \quad [38]$$

where  $L_v$  is the latent heat of evaporation,  $L_f$  is the latent heat of fusion,  $q_v$  is the mixing ratio of water vapor,  $q_{ice}$  is the mixing ratio of ice condensates, and  $T$  is the temperature.

The vertically integrated  $h$  ( $\hat{h}$ ) has appealing properties, including that it remains conserved during convective transport. The only sources for  $\hat{h}$  in the atmosphere are net column longwave radiative flux convergence (NetLW), net column shortwave radiative flux convergence (NetSW), latent heat flux (LHF), and sensitive heat flux (SHF). The only sink of  $\hat{h}$  is the horizontal divergence of  $\hat{h}$  flux.

In other words, the MSE budget equation is,

$$\frac{\partial \hat{h}}{\partial t} = LHF + SHF + NetLW + NetSW - \nabla_h \cdot \vec{u}\hat{h}, \quad [39]$$

Subtracting the domain mean from Equation 39 results in a budget equation for the time evolution of the anomalies in vertically integrated MSE,

$$\frac{\partial \hat{h}'}{\partial t} = LHF' + SHF' + NetLW' + NetSW' - \nabla_h \cdot \vec{u}\hat{h}, \quad [40]$$

where  $'$  represents the anomaly of each field with respect to the domain mean.

The MSE variance budget equation can be obtained by multiplying Equation 40 with  $\hat{h}'$ ,

$$\frac{1}{2} \frac{\partial \hat{h}'}{\partial t} = \underbrace{\hat{h}' LHF' + \hat{h}' SHF'}_{SEFContribution} + \underbrace{\hat{h}' NetLW' + \hat{h}' NetSW'}_{RadiativeContribution} - \nabla_h \cdot \vec{u}\hat{h}, \quad [41]$$

where SEF (the Surface Enthalpy Flux) is the sum of LHF (the Latent Heat Flux) and SHF (the Sensible Heat Flux). The radiative contribution consists of net column longwave radiative flux convergence (NetLW) and net column shortwave radiative flux convergence (NetSW). Primes are used to indicate anomalies relative to the mean of the spatial domain, which is represented by overlines. MSE spatial variance source terms are obtained by spatially averaging all terms on the right-hand side of Equation 41.

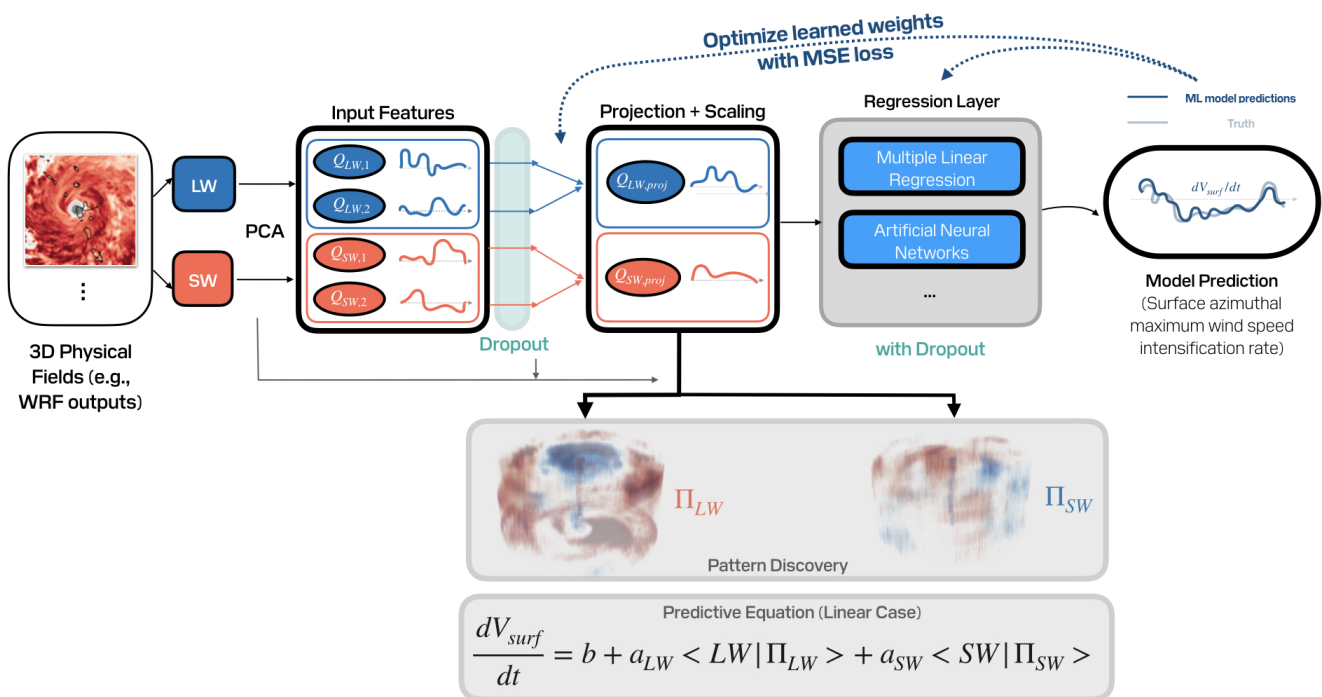


**Fig. S1.** The interpretable linear model baseline to compare to the VED model. This baseline model introduces uncertainty with the dropout operation.

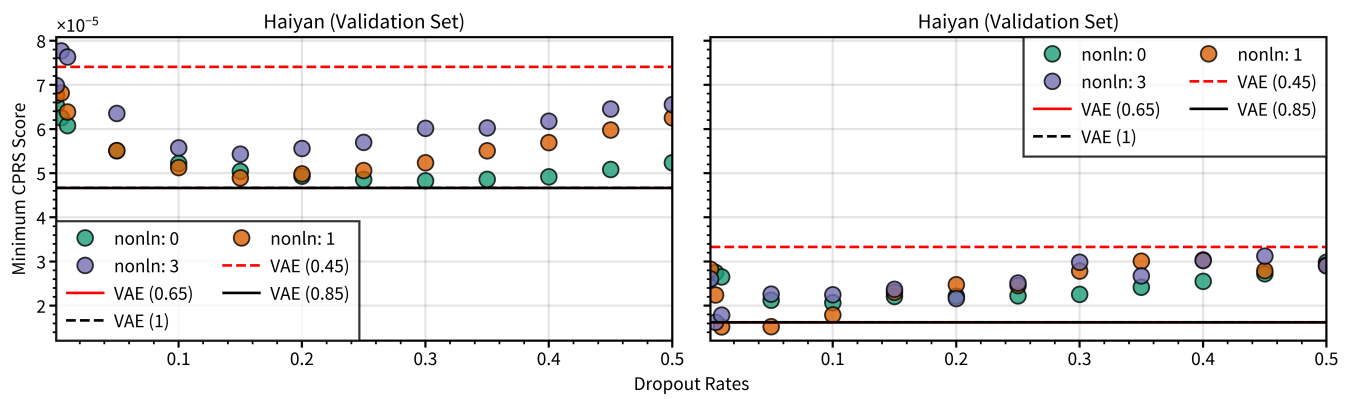


**Fig. S2.** The median (left) and minimum (right) CRPS scores for the baseline and VED models on the validation sets. The effect of nonlinearity on the baseline models is tested by adding 1, 3, or 5 regression layers with Rectified Linear Unit (ReLU) activation functions. Both types of models exhibit an optimal range of hyperparameters that would result in the best skill scores. However, the best VED model overperforms the best baseline model.

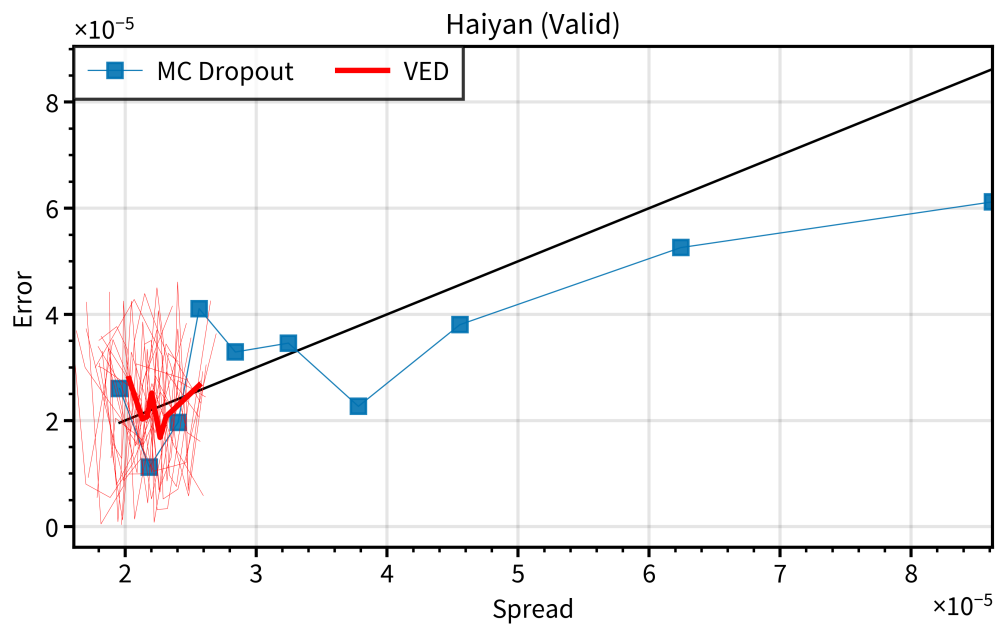


**Fig. S3.** Mean spread-skill curves for the best-performing baseline model (black) and the best-performing VED model (red thick). The VED curves for individual predictions with different random seeds are shown to show the prediction spread captured by the VED model.

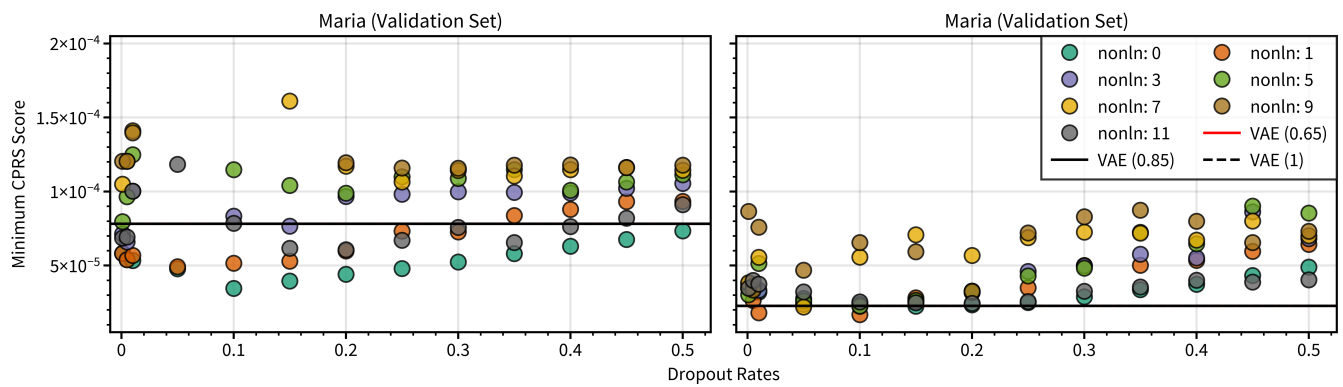


**Fig. S4.** CRPS performance diagram for the Maria validation set. For Maria, we tested the effect of adding nonlinearity up to 11 nonlinear regression layers.

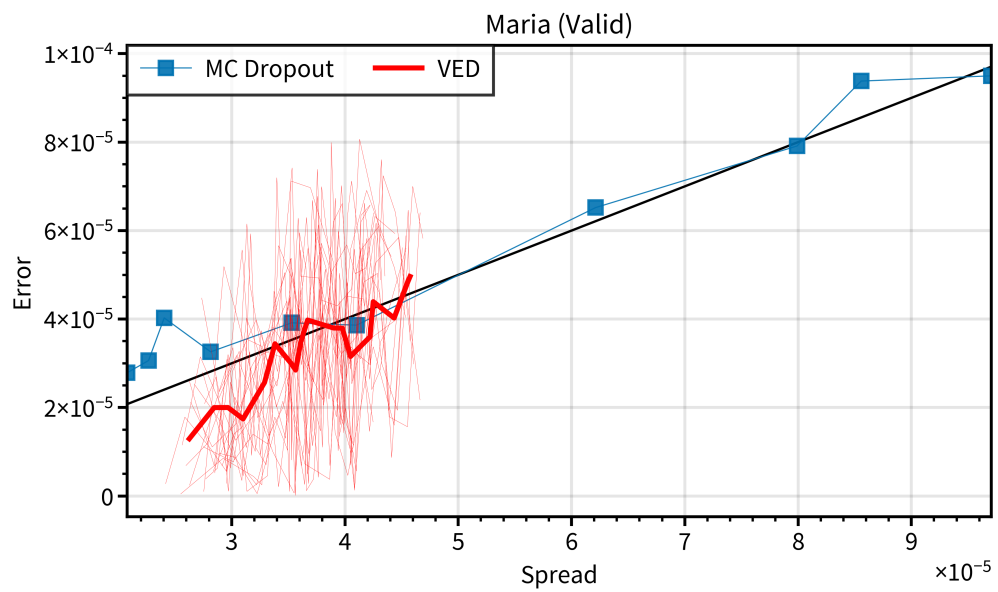


**Fig. S5.** The best-performing VED model for Maria is less accurate than the best Haiyan model on their corresponding validation set. However, the VED model somewhat outperforms the baseline model, especially regarding prediction errors.

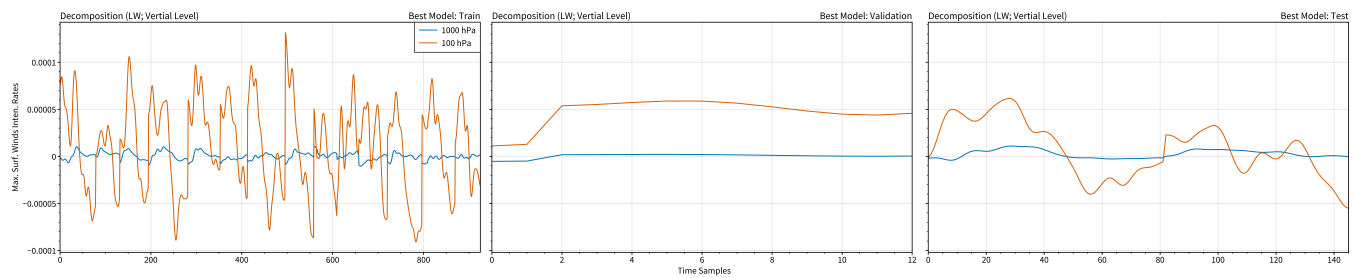


**Fig. S6.** Linear decomposition of the longwave contribution to the intensification of Haiyan. The contribution of upper-level radiative anomalies is consistently larger than the contribution of the low-level radiative anomalies.

**Table S1. Prediction skills of the best VED and the best baseline model on the intensification of Haiyan. Also shown in the table are the median skills of all trained models (numbers in brackets). All values in the table are multiplied by  $10^5$  for visualization purposes. The best model is illustrated with bolded numbers.**

Experiment	Metric	Training	Validation	Test
VED	CRPS	<b>2.83</b> (3.35)	<b>1.65</b> (4.69)	<b>2.86</b> (3.73)
	SSREL	<b>1.31</b> (2.61)	<b>0.33</b> (3.54)	<b>1.03</b> (2.44)
	RMSE	<b>4.52</b> (5.34)	<b>2.61</b> (6.99)	<b>4.83</b> (5.95)
	MAE	<b>3.67</b> (4.25)	<b>2.15</b> (5.76)	<b>3.75</b> (4.74)
Baseline	CRPS	3.23 (3.48)	2.26 (4.83)	3.45 (3.90)
	SSREL	1.89 (2.45)	0.67 (4.19)	1.17 (2.76)
	RMSE	5.35 (5.68)	3.67 (7.17)	5.54 (6.09)
	MAE	4.28 (4.56)	2.96 (6.00)	4.31 (4.93)

**Table S2. Prediction skills of the best VED and the best baseline model on the intensification of Maria.**

Experiment	Metric	Training	Validation	Test
VED	CRPS	1.76 (5.88)	<b>2.28</b> (7.78)	<b>1.39</b> (5.26)
	SSREL	0.59 (3.51)	<b>0.80</b> (4.33)	<b>0.33</b> (2.95)
	RMSE	3.74 (9.27)	3.93 (10.12)	<b>2.21</b> (7.32)
	MAE	2.21 (7.95)	3.20 (9.95)	<b>1.74</b> (7.08)
Baseline	CRPS	<b>1.16</b> (2.32)	2.39 (3.46)	2.32 (2.60)
	SSREL	<b>0.36</b> (1.62)	0.88 (3.28)	1.68 (2.21)
	RMSE	<b>2.46</b> (4.57)	<b>3.57</b> (6.22)	3.54 (3.84)
	MAE	<b>2.03</b> (3.21)	<b>3.13</b> (4.85)	3.22 (3.51)

**Table S3. Characteristics of the data splits used for training the Haiyan models. Ensemble Members that are not numbered in the table are treated as training sets.**

Data split	Validation		Test		Data split	Validation		Test	
1	11	4	10	17	20	16	11	10	17
2	11	7	10	17	21	16	12	10	17
3	12	13	10	17	22	18	11	10	17
4	12	14	10	17	23	18	1	10	17
5	12	6	10	17	24	18	3	10	17
6	13	19	10	17	25	19	1	10	17
7	13	7	10	17	26	19	7	10	17
8	14	12	10	17	27	19	8	10	17
9	14	18	10	17	28	1	11	10	17
10	14	19	10	17	29	1	5	10	17
11	14	4	10	17	30	1	9	10	17
12	14	6	10	17	31	2	19	10	17
13	14	7	10	17	32	2	7	10	17
14	15	13	10	17	33	3	19	10	17
15	15	16	10	17	34	3	1	10	17
16	15	19	10	17	35	4	6	10	17
17	15	5	10	17	36	5	19	10	17
18	15	7	10	17	37	6	1	10	17
19	15	8	10	17	38	7	14	10	17
39	7	3	10	17	40	7	5	10	17

## References

1. A Paszke, et al., Pytorch: An imperative style, high-performance deep learning library (2019).
2. T Akiba, S Sano, T Yanase, T Ohta, M Koyama, Optuna: A next-generation hyperparameter optimization framework (2019).
3. DP Kingma, M Welling, Auto-encoding variational bayes (2022).
4. A Alemi, et al., Fixing a broken ELBO in *Proceedings of the 35th International Conference on Machine Learning*, Proceedings of Machine Learning Research, eds. J Dy, A Krause. (PMLR), Vol. 80, pp. 159–168 (2018).
5. K Haynes, R Lagerquist, M McGraw, K Musgrave, I Ebert-Uphoff, Creating and evaluating uncertainty estimates with neural networks for environmental-science applications. *Artif. Intell. Earth Syst.* **2**, 220061 (2023).
6. L Delle Monache, FA Eckel, DL Rife, B Nagarajan, K Searight, Probabilistic weather prediction with an analog ensemble. *Mon. Wea. Rev.* **141**, 3498–3516 (2013).
7. AA Wing, KA Emanuel, Physical mechanisms controlling self-aggregation of convection in idealized numerical modeling simulations. *J. Adv. Model. Earth. Syst.* **6**, 59–74 (2014).